

Topographic Effects on Internal Waves in Barkley Canyon

Kurtis Anstey

V00939802

Department of Physics and Astronomy

University of Victoria

October 2, 2021

Dr. Jody Klymak (University of Victoria)

Dr. Steven Mihaly (Ocean Networks Canada)

Dr. Richard Thomson (Institute of Ocean Sciences)

Table of Contents

List of Figures	3
1 Abstract	4
2 Introduction	5
3 Theory	8
4 Data	11
5 Results and discussion	16
5.1 Observations	16
5.2 Depth dependence	20
5.3 Frequency dependence and seasonality	21
5.3.1 Sub-diurnal	23
5.3.2 Diurnal	23
5.3.3 Near-inertial	25
5.3.4 Semidiurnal	29
5.3.5 Continuum	32
6 Summary and conclusions	35
7 Appendix A: Frequency band comparisons	37
8 References	41

List of Figures

1	Internal wave processes	6
2	Internal waves in a two-layer system	8
3	Radiating internal waves in a lab	10
4	Internal waves and topography	11
5	Barkley Canyon site map and semidiurnal criticality	12
6	ADCP frequency, deployment, and data availability	13
7	Site topography	14
8	Averaged stratification and WKB scaling	15
9	Velocities - 2013	17
10	PSD and rotary spectra - 2013	19
11	Depth-frequency - 2013	22
12	Diurnal spring-neap forcing	24
13	Seasonal mixed-layer depth	25
14	Mixed-layer currents and flux	26
15	Mixed-layer near-inertial forcing comparison	27
16	Lack of near-inertial blue-shift	29
17	Semidiurnal spring-neap forcing	30
18	Continuum <i>a</i> and <i>b</i> time series	32
19	Continuum GM comparison	33
20	Dissipation and diffusivity	34
21	Depth-band PSD - Upper Slope - 2013	37
22	Depth-band PSD - Axis - 2013	38
23	Depth-band rotary spectra - Upper Slope - 2013	39
24	Depth-band rotary spectra - Axis - 2013	40

1 Abstract

We make use of four overlapping years of ADCP horizontal velocity time-series data near Barkley Canyon, from both slope and canyon sites, to examine the effects of variable topography on the local internal wave field. Results indicate there is frequency dependent focusing of spectral power near topography, up to $1.5\times$ orders of magnitude 150 m above the continental slope, and up to $2\times$ orders of magnitude 250 m above the canyon bottom, with unique seasonality for individual constituents. Sub-diurnal and diurnal flows are sub-inertially trapped along topography and appear to be forced locally (barotropically), while free semidiurnal internal tides are focused and reflected near critical topography and appear to experience both local and remote (baroclinic) forcing. The near-inertial band is attenuated near the slope, and enhanced near the canyon bottom, with intermittent forcing that appears linked to regional wind events. Finally, a near-topography enhanced internal wave continuum (over $3\times$ GM on the slope, and $5\times$ GM in the canyon) indicates increased rates of dissipation (exceeding 10^{-8} W/kg near the slope, and 10^{-7} W/kg in the canyon) and diffusivity (exceeding 10^{-3} m²/s near the slope, and 10^{-2} m²/s in the canyon), with seasonality suggesting a cascade of energy from low-frequency constituents (tidal on the slope, and near-inertial in the canyon) to high-frequency dissipative processes.

2 Introduction

Internal waves are slow-moving, low-frequency, sub-surface gravity waves that exist within density gradients in the ocean interior (Garrett & Munk, 1979). They have wavelengths up to kilometres long, and oscillate in a range between the local Coriolis (inertial, f) and Brunt–Väisälä (buoyancy, N) frequencies (Garrett & Munk, 1979). They are forced by weather - as near-inertial internal waves are generated by surface winds exciting currents in the mixed layer that 'pump' energy into the internal wave field, below (Garratt, 1977) - or by tides and currents moving over irregular seafloor topography, generating baroclinic waves that can propagate through the stratified ocean (Hendershott & Garrett, 2018). Nonlinear interactions with irregular topography can cause incident internal waves to scatter, reflect, or focus and break, leading to mixing (Martini et al., 2013).

As the wind and tides are ever-present, internal waves are prevalent ocean phenomena. As early as the mid-19th century, scientists such as Stokes and Rayleigh were investigating properties of fluid density and stratification, essential for internal wave propagation (Garrett & Munk, 1979). Internal waves were mistaken as consistent noise in early 20th-century hydrocast readings, and Ekman discussed their effects in his seminal theories on fluid mechanics (Garrett & Munk, 1979). In the late-20th century, Garrett and Munk (1979) developed the canonical Garrett-Munk (GM) spectrum defining the characteristic frequency and wavenumber continuum of open-ocean internal waves, to better understand their role in ocean processes. As instrumentation improves, scientists continue to uncover the contributions of internal waves to both small- and large-scale physical systems, such as mixing and circulation (Figure 1; Garrett & Munk, 1979). Recent studies have focused on internal wave generation and dissipation (Terker et al., 2014; Kunze, 2017), forcing response and seasonal variability (Alford et al., 2012; Thomson & Krassovski, 2015), and the prevalence of boundary layer mixing due to interactions of internal waves with irregular topography (Nash et al., 2004; Kunze et al., 2012; Gemmrich & Klymak, 2015).

As internal waves and tides approach seamounts, slopes, or canyons, their energy is focused and can cascade from low- to high-frequency processes, eventually dissipating as heat (Garrett & Munk, 1979). Dissipation leads to an energetic local environment, evident as turbulent processes on the fine- (1 – 100 m vertical) and micro-scales (< 1 m vertical) (Garrett & Munk, 1979; Kunze et al., 2012). These processes drive regional transport of energy and momentum, and the mixing of heat, pollutants, and biological constituents (Kunze et al., 2012). Furthermore, topography-forced internal wave mixing

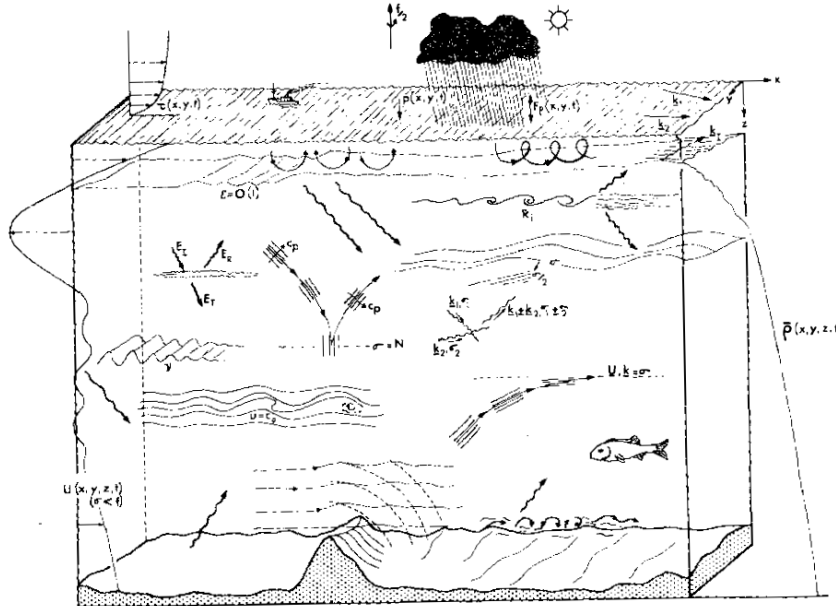


Figure 1: Generalised depiction of internal wave processes in the ocean, as envisioned by Garrett and Munk (1979). Internal waves are forced by, coincide with, or contribute to most physical processes in the ocean.

helps to set ocean stratification, layers that drive large-scale physical systems such as the overturning circulation (Garrett & Munk, 1979). As such, knowledge of topography-internal wave interactions is important for understanding both regional dynamics and the coupled ocean-atmosphere climate system (Garrett & Munk, 1979).

Topography focused internal wave studies are global, ongoing at locations such as the Hawaiian ridge (Alford et al., 2007), the continental slopes of the South China Sea (Klymak et al., 2011), and the slope-incising submarine canyons of the northeast Pacific (Allen et al., 2001; Carter & Gregg, 2002; Kunze et al., 2012; Terker et al., 2014). Canyons and their adjacent continental slopes have been identified as hot spots of internal wave activity, that both generate (Carter & Gregg, 2002) and dissipate (Allen et al., 2001; Kunze et al., 2002) internal waves and tides. Research at Monterey Canyon has produced results regarding the scattering and reflection of internal waves and tides on critical slopes (Figure 4; Kunze et al., 2012), the presence of near-bottom turbulent layers that drive mixing (Carter & Gregg, 2002; Kunze et al., 2002), and a correlation between topography and increased dissipation and generation (Terker et al., 2014). Further research on internal wave interactions

with submarine canyons and their adjacent continental slopes is thought to be essential to understanding enhanced upwelling, diapycnal mixing, and cross-shelf exchange, drivers of dynamic regional and large-scale processes (Burrier, 2019).

In Canada, research in the Pacific is often focused on the highly productive Vancouver Island Continental Shelf (VICS) (Allen et al., 2001), a relatively broad (about 80 km) shelf region with a canyon-incised continental slope. Physically, regional internal wave studies have led to insight on seasonal wind forcing for near-inertial internal waves (Alford et al., 2012), non-linear wave-wave interaction between near-inertial internal waves and semidiurnal internal tides (Mihaly et al., 1998), and locally generated baroclinic shelf waves of diurnal frequency (Thomson & Crawford, 1982). Seasonally variable regional currents (Thomsons & Krassovski, 2015) have been associated with observations of vorticity stretching and upwelling at the head of the shelf-incising Barkley Canyon, suggesting considerable canyon influence on local water properties, transport of biological constituents, and overall shelf productivity (Allen et al., 2001; Juniper et al., 2013; Doya et al., 2013; Chauvet et al., 2018).

However, despite the considerable body of ocean research on the VICS, there is a lack of topography-internal wave interaction knowledge necessary to fully understand the driving physical dynamics. Further research into Barkley Canyon and slope induced internal wave mixing can not only provide insight into the high productivity of the VICS, but an additional case study for topography driven internal wave research, globally.

Building on prospective research by Burrier (2019), this study evaluates horizontal velocity data from two sites, one within Barkley Canyon and another on the adjacent continental slope, to characterise the presence of internal waves and tides, their interactions with topography, and potential influence on local mixing. Sub-tidal, tidal, near-inertial, and high-frequency internal wave bands are evaluated for depth-dependence and seasonality, including a forcing analysis of variability in regional mean currents, tides, and wind. Finally, the state of the high-frequency internal wave continuum is evaluated for topographic enhancement through comparison with accepted GM theory, and estimates of dissipation and diffusivity to estimate mixing contributions. Key findings include near-topography enhancement of internal wave power with frequency-dependent seasonality, near-inertial internal wave attenuation near the continental slope with intermittent forcing from wind events and mixed-layer depth, and a heightened high-frequency continuum state with seasonality suggesting a cascade of energy from low-frequency constituents to high-frequency dissipative processes.

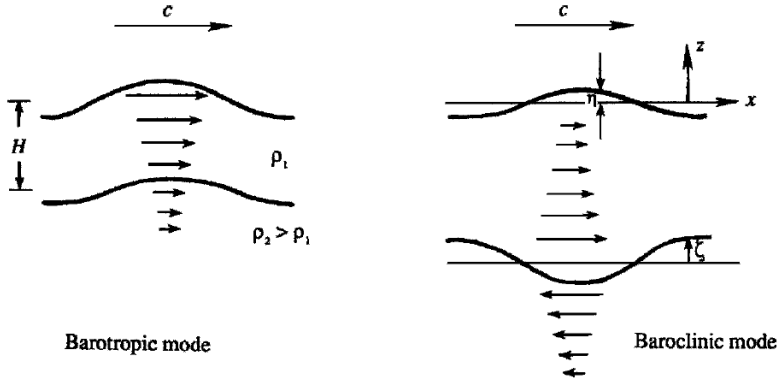


Figure 2: Internal waves in a two-layer system. Graphic representation of the difference between barotropic and baroclinic flow. Adapted from Kundu & Cohen (2008).

3 Theory

Much of the following is adapted from a much more detailed discussion by Kundu & Cohen (2008), and the reader is encouraged to seek out this foundational text.

Internal waves are dependent on stratification that increases near topography and the surface, but do not require a sharp density interface to exist; they are commonly found in continuously stratified fluids like the ocean interior, where density, $\rho(z)$, is a function of depth, z . In order to describe the oscillatory motion of a fluid parcel displaced vertically in a continuously stratified medium, it is necessary to introduce the buoyancy frequency, N , as:

$$N^2(z) = -\frac{g}{\rho_0} \frac{\partial \rho(z)}{\partial z} \quad (1)$$

where g is the acceleration due to gravity, and ρ_0 is a reference density at a particular depth. Buoyancy effects allow for internal wave propagation through a continuously stratified fluid, and suggest that internal waves are non-isotropic. Thus, for a 2D approximation, wavenumber (k and m), frequency (ω), and phase and group velocities (c_p and c_g) are vector quantities, due to the importance of both magnitude and direction.

Furthermore, internal waves in a continuously stratified fluid are rotational. This further necessitates a dispersion relation with appropriate buoyancy considerations in vector form. However, as N varies with depth, this is difficult. If $N(z)$ is allowed to change with depth, vertical propagation of internal

waves can be limited at 'turning depths'. The effect is better described by the Wentzel–Kramers–Brillouin (WKB) approximation, where for a single propagating wave ω and k are held fixed, while N is free to adjust to an adaptive vertical wavenumber, m (Garrett & Munk, 1979). For an elementary model (not observationally), it is found that the vertical change in N is slow enough, locally, that as a final leading assumption N can be considered depth independent.

With these considerations, for a steady stratified flow the vertical velocity, w , is:

$$w = w_0 e^{i(kx + mz - \omega t)} \quad (2)$$

where w_0 is an amplitude, x the horizontal distance, and t is time. Some algebraic work results in a surprisingly simple expression for the dispersion relation, as:

$$\omega = N \cos(\theta) \quad (3)$$

where θ is the angle from the horizontal axis to the direction of the phase velocity, c_p . This suggests that the frequency of internal waves only depends on the direction of the wavenumber (in θ), and also that N is the limiting maximum frequency of internal waves. The maximum frequency of $\omega_{\max} = N$ is found at the limit of $\theta = 0$, when the wavenumber is purely horizontal, i.e. $m = 0$, so that the water column oscillates vertically. Similarly, and again considering rotation effects, it is found that the limiting minimum frequency for internal waves, ω_{\min} , is the local Coriolis parameter, f (Garrett & Munk, 1979).

As a result of the directional dispersion relation, the group velocity, c_g , is found to be perpendicular to the phase speed, c_p ; i.e. the \mathbf{e}_1 components are the same, while the \mathbf{e}_3 components are opposite. This is interesting in that crests of phase propagate perpendicularly away from the beam of energy propagation associated with group velocity. It follows that in 2D, internal waves radiate group velocity outward from a source in four directions, each at an angle θ from vertical (Figure 3). This angle is defined by $\cos(\theta) = \omega/N$, with one beam in each quadrant, and phase radiating perpendicularly outward from each. From this result it follows that the energy flux per unit area is $F = c_g E$, where E is the energy per unit volume.

For field observations (where N is depth-dependent) of free internal waves and tides incident upon irregular topography (continental slopes, canyons, etc.), the angle of the incident wave energy, α , and the slope of the topography, β , have an influential relationship on the behaviour of the interaction (Figure 4) (Lamb, 2014). The angle of propagation of an incident, free internal wave in

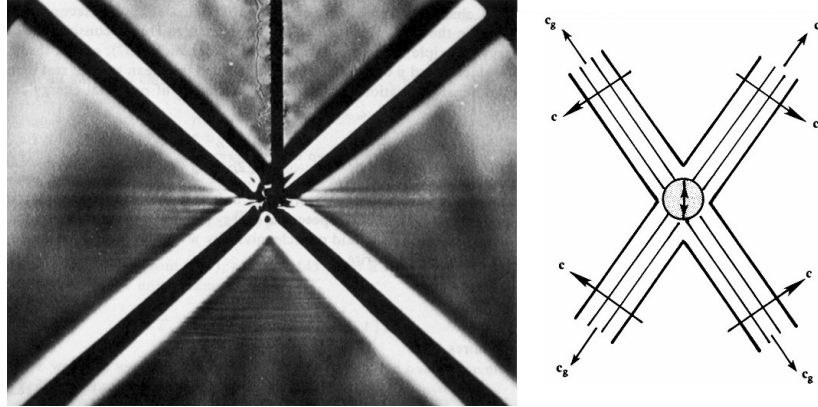


Figure 3: A photograph and graphic showing laboratory evidence for the radiation of 2D internal waves, from a source. Note the perpendicular phase and group velocities, and distinct propagation angles. Adapted from Kundu & Cohen (2008).

a continuously stratified fluid is:

$$\alpha(z) = \sqrt{\frac{(\omega^2 - f^2)}{(N(z)^2 - \omega^2)}} \quad (4)$$

where ω is the frequency of the incident wave (Lamb, 2014). The bathymetric slope, $\beta = \nabla H$, is determined from the gradient magnitude of the local topography, and used to determine regions of slope criticality, as in Figure 5 (Martini et al., 2011). To generalise, if $\beta > \alpha$ the slope is considered supercritical and incident wave energy is reflected back down into the ocean basin (see Figure 7); for $\beta \approx \alpha$ the slope is considered near-critical and incident wave energy is focused, potentially leading to non-linear breaking events; and, for $\beta < \alpha$ the slope is considered subcritical and incident wave energy is scattered upward into shallow shelf waters (Klymak et al., 2011).

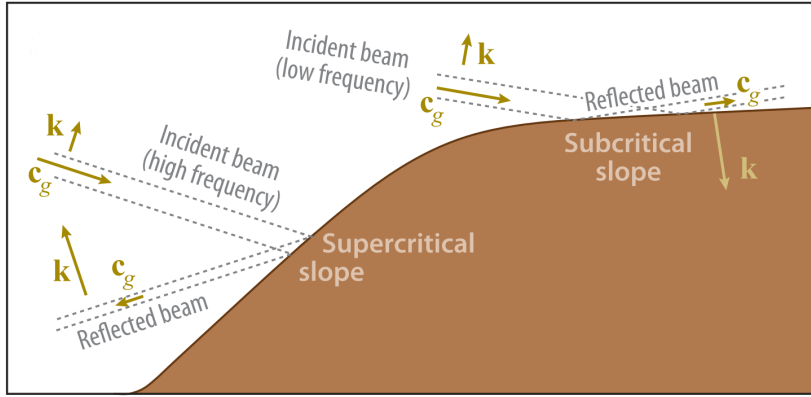


Figure 4: Graphic of internal wave interactions with slope topography (Lamb, 2014). The propagation angle of an internal wave depends on frequency and stratification. Depending on the slope of topography, incident internal waves can be scattered up, reflected down, or focused, possibly breaking.

4 Data

The Barkley Canyon velocity data is unique for both temporal and spatial considerations. Located at approximately 48.33°N 126.03°W, Barkley Canyon is about 75 km southwest of the coast of Vancouver Island, incising the continental slope (Figure 5; Barkley Canyon, 2013). Spread across the local topography, Acoustic Doppler Current Profilers (ADCP) and other instruments provide current data for Ocean Networks Canada's (ONC) NEPTUNE cabled observatory (2013). ADCP emit acoustic beams that triangulate Doppler shifts in the water column, providing time series of directional velocity data through depth. The ADCP and their data are operated, maintained, and cleaned for public distribution by ONC; the Oceans 2.0 data portal offers publicly available data spanning over a decade, from 2009 to present. This is substantially lengthy dataset for internal wave research, allowing for typically difficult analysis of long-term variability.

Relevant ADCP were chosen at both the upper continental slope 'Upper Slope' (Slope) and the canyon-bottom 'Axis' sites (Figure 5), 15 km apart, to allow for spatial analysis of simultaneous internal wave interactions at varied topography. The 75 kHz Slope instrument sits below the VICS shelf-break at a depth of -378 metres (Figure 7), 15 km NW of Barkley Canyon. The 75 & 55 kHz Axis instruments are located at a narrow north-south channel in Barkley Canyon, about midway along its length at a sharp bend, at a depth of -968

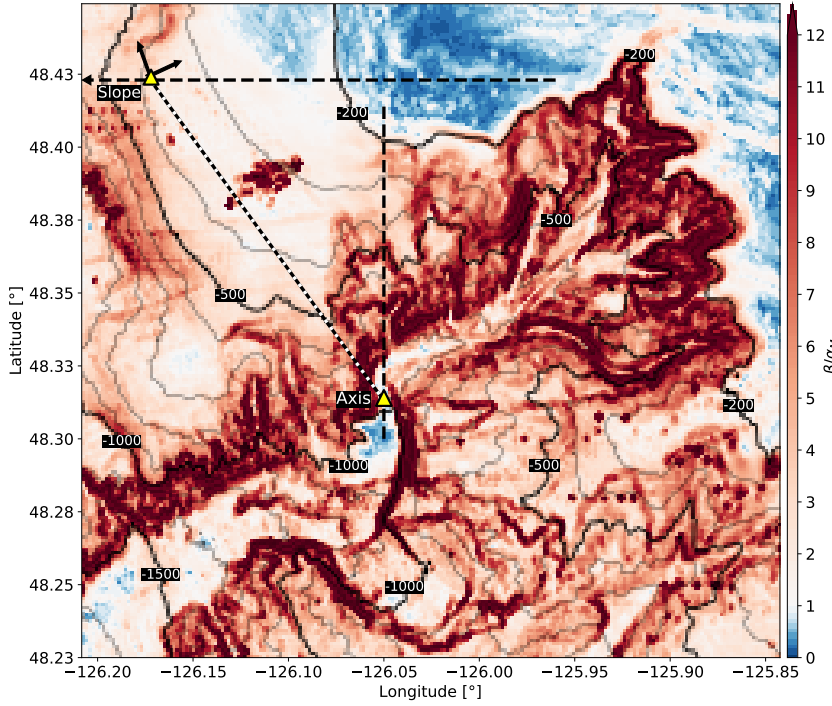


Figure 5: Site map and semidiurnal criticality of Barkley Canyon. Criticality is found by dividing the gradient slope (β) of topography by the depth-dependent semidiurnal propagation angle (α_{M2}). Most of the region is supercritical (> 1) to the M_2 internal tides, with notable exceptions on the shelf and canyon floor near the Axis site. Arrows at the Slope site indicate 30° rotation of velocity data to match approximate along-slope (v) direction of mean currents; Axis data were not rotated, as the along-canyon (v) component is aligned N-S. Dashed black lines indicate topography cross-sections used in Figure 7, and the dotted black and white line represents the 15 km horizontal distance between sites.
ADJUST QUALITY FOR FINAL DRAFT.

metres (Figure 7). The 75 kHz Teledyne RDI Workhorse Long Ranger instruments have a vertical resolution of 8 m depth bins, and a continuous sampling rate of 2 seconds. The 55 kHz Nortek Signature55 instrument has a vertical resolution of 20 m depth bins, and a pulsed sampling rate of six 18-second pings followed by a 4.5-minute delay.

To assess data quality and coverage, an initial quality check of error velocity, correlation, and backscatter intensity for both depth and time - based on ONC deployment parameters - was performed with the raw 2-second data.

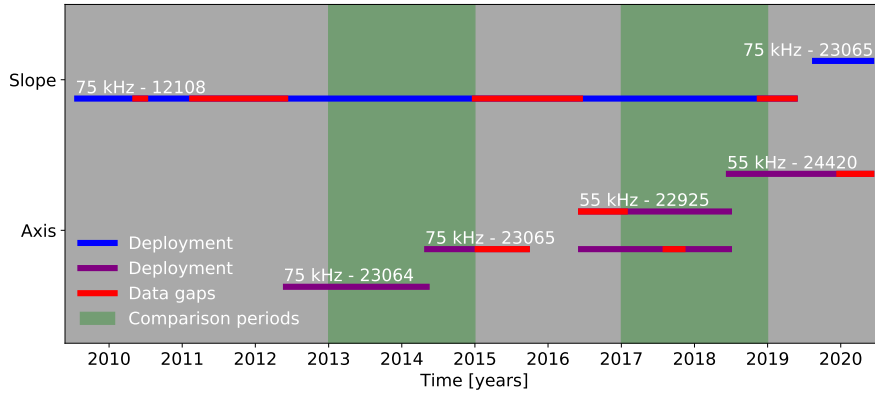


Figure 6: ADCP operating frequency, deployment periods, and data availability for the Slope and Axis sites. ONC operates and maintains regional instruments as part of the NEPTUNE cabled observatory. Due to maintenance and redistribution, years with comprehensive overlapping coverage (2013, 2014, 2017, and 2018) were chosen for analysis, with 2013 as the reference year for discussion, as described in Section 4.

For Slope, the primary analysis region is below -50 m to avoid mixed-layer turbulence, and at Axis below -650 m to avoid instrument range limitations. The unanalysed upper depths are retained in plots, for reference.

Complete datasets for Slope and Axis were acquired in NetCDF format at an averaged temporal resolution of 15-minutes, deemed adequate for the science objectives of this research. Overlapping data coverage of good quality (e.g. minimal data gaps) is primarily during 2013, 2014, 2017, and 2018, and these years were chosen to provide the bulk of the inter-annual analysis (Figure 6). There is little observed variability between years beyond certain intermittent forcing (e.g. wind), to be discussed in Section 5.3. To be concise regarding such a large dataset, the majority of the results discussion will focus on 2013 as an indicative reference year, with inter-annual observations available for reference, along with the Python code and supplemental figures and analysis, in the project GitHub repository hosted at <https://www.github.com/kurtisanstey/project/>.

For preliminary data management the segmented datasets were combined for each instrument, and mapped to a standard set of depth bins for consistency of analysis. NaN values were interpolated using a linear process for gaps less than 25 hours. To deal with larger data gaps, the datasets were subdivided

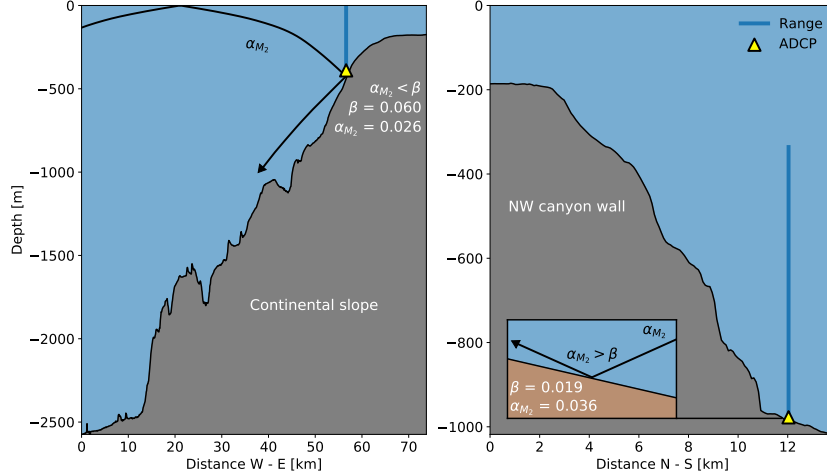


Figure 7: Site topography cross-sections with ray tracing. Depicted are the relative locations for Slope (left) and Axis (right) instrument moorings. Horizontal cross-sections were taken in the W-E (Slope) and N-S (Axis) directions, represented by the dashed black lines in Figure 5. Slope sits below the VICS shelf-break while Axis is located on the floor of Barkley Canyon (right). An incident ray is shown for M_2 , accounting for depth-dependent stratification, as well as local criticality at each site. α is the angle of propagation, and β is the slope of the topography. In general, the Slope region is supercritical, while the Axis region is both subcritical (floor) and supercritical (walls).

by year and section, and combined as needed, using weighted averaging when necessary.

At Slope, velocity data were rotated using a standard rotation matrix as:

$$u_{rot} = u\cos(\theta) - v\sin(\theta) \quad (5)$$

$$v_{rot} = u\sin(\theta) + v\cos(\theta) \quad (6)$$

where θ is the rotation angle in radians. This was done to better match the cross-slope angle of approximately $+30^\circ$, to help identify relationships between the predominant VICS currents and local topography; u is referred to as 'cross-slope', and v is 'along-slope' (Figure 5). At the Axis site, the along-canyon (v) direction is approximately north-south, so no rotation was necessary; as such, u at Axis is referred to as cross-canyon.

Finally, to account for the effects of observed stratification, horizontal velocity

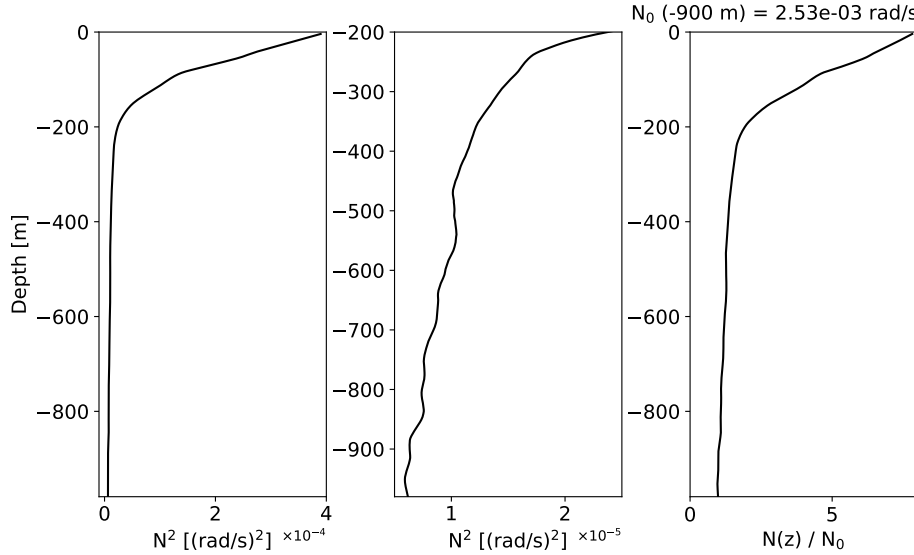


Figure 8: N^2 parameter and WKB scaling factor. Buoyancy results were smoothed then averaged from 10 years of La Perouse station LB14 CTD data, and are displayed through the water column (left) and below -200 m (centre). Depth-dependent buoyancy versus reference buoyancy (right) was determined for use in Equation 8, based on N_0 averaged around -900 m.

data were WKB-scaled according to:

$$u_{WKB}(z) = u(z) \sqrt{\frac{N_0}{N(z)}} \quad (7)$$

and for energy density as:

$$\phi_{WKB}(z) = \phi(z) \frac{N_0}{N(z)} \quad (8)$$

with a reference buoyancy frequency of $N_0 = 2.53 \times 10^{-3}$ rad/s averaged around -900 m (Althaus et al., 2003). Buoyancy data were determined from conductivity-temperature-depth (CTD) climatology data obtained from the nearby (21 km SE) station LB14, sampled annually May and September during Fisheries and Oceans Canada (DFO) operated La Perouse research cruises, casting down to -1180 m. From the CTD data, depth profiles were obtained for temperature, $T(z)$, pressure, $P(z)$, and salinity, $S(z)$, used to find potential

density, $\rho_\theta(z)$, following the UNESCO 1983 (EOS 80) polynomial. The depth-dependent buoyancy frequency was then determined as in Equation 1 (Figure 8).

5 Results and discussion

5.1 Observations

Regional low-frequency mean currents are seasonally site-dependent and topographically guided, along-slope at Slope and along-canyon at Axis (Figure 9). To identify long-term mean currents, a 40-hour, 8th-order, digital low-pass Butterworth filter was applied to the adjusted (as in Section 4) and WKB-scaled horizontal velocity data. At Slope, currents below -50 m are as expected for this portion of the California current system (Thomson et al., 2015): generally poleward along-slope through depth, with a quick transition to upwelling-favourable equatorward flow in the late-spring (April/May), and the deep poleward currents pushing back to the surface by fall. At Axis, mean currents below -650 m are prominently up-canyon, with some down-canyon flow directly above bottom (AB), strongly suggesting topographic guidance by the canyon, and showing little apparent seasonality. Mean currents at Slope (over 0.1 m/s) are more than twice as strong as compared to Axis (up to about 0.05 m/s).

Higher-frequency velocity data show variability in constituent internal waves and tides. Subtracting the low-pass currents from the total yields residual 'high-pass' currents - flows with periodicity less than 40-hours (Figure 9). A two-week snapshot of the higher-frequency velocities during the recurring April/May mean-current transition reveals the presence of internal waves and tides of various frequencies and non-uniform vertical structure, suggesting some baroclinic forcing. There is little intra-annual variability. At the Slope site, high-pass currents reach over 0.1 m/s in both cross- and along-slope directions, suggesting less topographic (along-slope) influence for shorter time-scale flows, and there is notable non-uniform vertical structure above -250 m depth (150 m AB). At Axis, high-pass currents are strongest below -750 m (250 m AB), up to about 0.2 m/s and mostly along-canyon, with increased non-uniformity in vertical structure above.

Power spectra indicate the high-pass velocities are primarily comprised of motions on diurnal, near-inertial, and semidiurnal frequencies. Component-wise power spectral densities (PSD) were determined from the adjusted (as in Section 4) and WKB-scaled horizontal velocity data, using a Welch method spectrogram process at each depth, with a Hanning window of 256 data-points (2.7

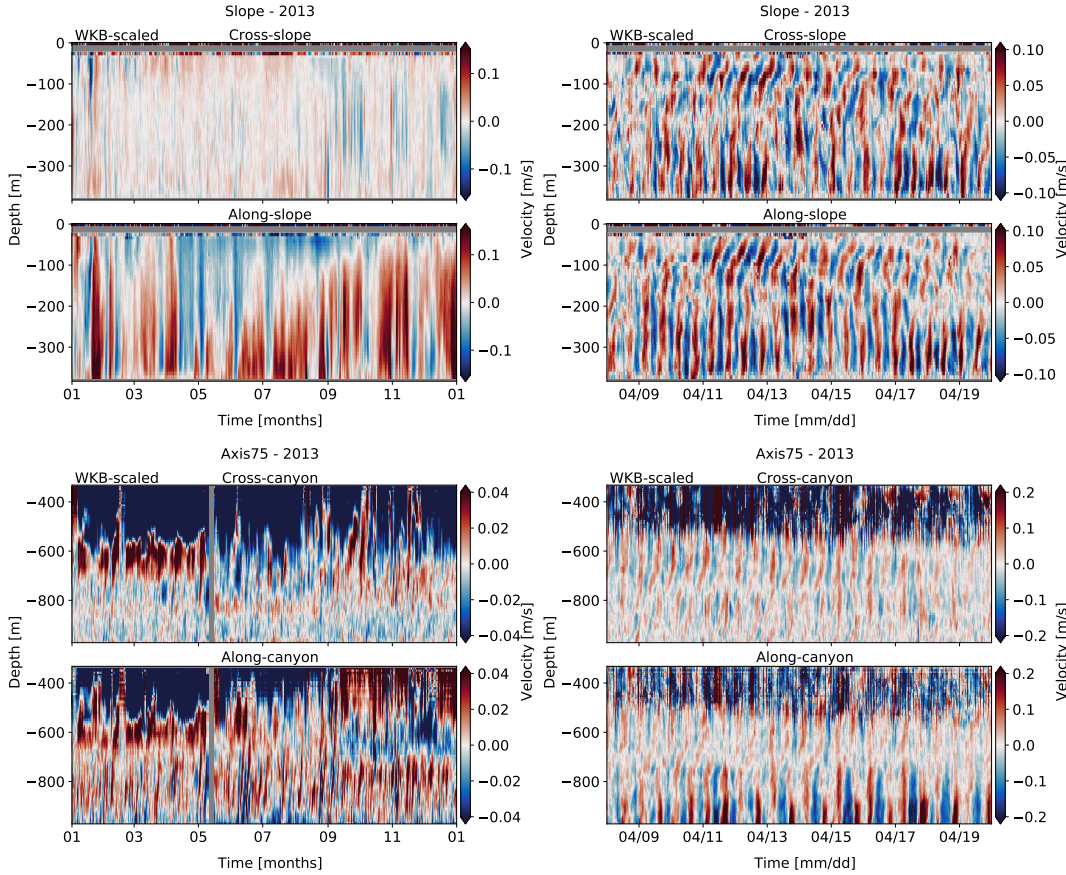


Figure 9: 40-hour low-pass (left) and high-pass (right) horizontal velocity data for Slope (top) and Axis (bottom), in 2013. For each site, components are separated as cross- (upper) and along-slope/canyon (lower). Velocities are 'adjusted', in that they have been rotated (Slope), NaN-interpolated, and WKB-scaled as detailed in section 4. In the low-pass, there is a clear seasonal cycle in the along-slope component at Slope, while seasonality is less apparent in the predominantly along-canyon flow at Axis. In the high-pass, there are internal waves and tides of varied frequency, non-uniform vertical structure, and depth-dependence - most notably near-bottom at Axis.

days) and a 50% overlap. For comparison, additional 'fine' (short window, poor frequency-resolution) and 'coarse' (long window, excellent frequency-resolution) time-resolution spectra were computed with 128 (1.3 days) and 512 (5.3 days) data-points, respectively. The noise floor of each instrument was determined from the standard error of the mean relative to instrument

deployment parameters (e.g. pings per sampling interval; ONC) and velocity uncertainties supplied by Nortek and RDI. 95% confidence intervals were determined using a chi² method. For comparison, local water properties were used to determine the local GM internal wave spectrum as it would appear for the open-ocean. The process was adapted from Callies (2016), using local parameters for Coriolis, $f = 1.73 \times 10^{-5}$ Hz, acceleration due to gravity, $g = 9.81(m/s)^2$, and N_0 , along with canonical values for the surface-extrapolated buoyancy frequency (5.24×10^{-3} rad/s), e-folding scale of $N(z)$ (1.3×10^3 m), mode scale number $j^* = 3$, and dimensionless internal wave energy parameter $E = 6.3 \times 10^{-5}$, following from Munk's seminal chapter in Wunsch's *Evolution of Physical Oceanography* (1981).

For rotational dependence, rotary power spectra were determined similarly to PSD, using an extended spectrogram process based on the work of Gonella (1972), and Thomson and Emery (2014) (Figure 10). To summarise, the adjustment to find the counter-clockwise (CCW) and clockwise (CW) components of a complex horizontal velocity vector, $\mathbf{w}(t) = u(t) + iv(t)$, is the addition or subtraction of its quadrature spectrum, Q_{uv} , as:

$$\text{CCW} = \frac{1}{2}[S_{uu} + S_{vv} + 2Q_{uv}] \quad (9)$$

$$\text{CW} = \frac{1}{2}[S_{uu} + S_{vv} - 2Q_{uv}] \quad (10)$$

where S_{uu} and S_{vv} are the typical complex autospectra used for PSD (Thomson & Emery, 2014). The directional GM spectrum was also adapted to rotary form, through application of the rotary consistency relation:

$$\frac{\text{CCW}}{\text{CW}} = \frac{(\omega - f)^2}{(\omega + f)^2} \quad (11)$$

to the directional GM kinetic energy spectrum (Levine, 2002; Polzin & Lvov, 2011). In general, a stronger CW component indicates downward propagation of energy, and vice-versa.

Annual mid-depth (-195 m and -800 m) power spectra at each site are characteristically red, and show strong tidal and near-inertial influence (Figure 10). Primary tidal constituents are of the diurnal (sub-inertial, 1.16×10^{-5} Hz) and semidiurnal (super-inertial, 2.24×10^{-5} Hz) frequencies. Closely associated constituents (such as S_2 and M_2) are not resolved, so the tidal peaks are referred to using their general descriptions (e.g. diurnal). The low-frequency 'sub-diurnal' broadband (below about 1×10^{-5} Hz) leads the tidal range, and the high-frequency internal wave 'continuum' (between 6×10^{-5} and 1×10^{-4}

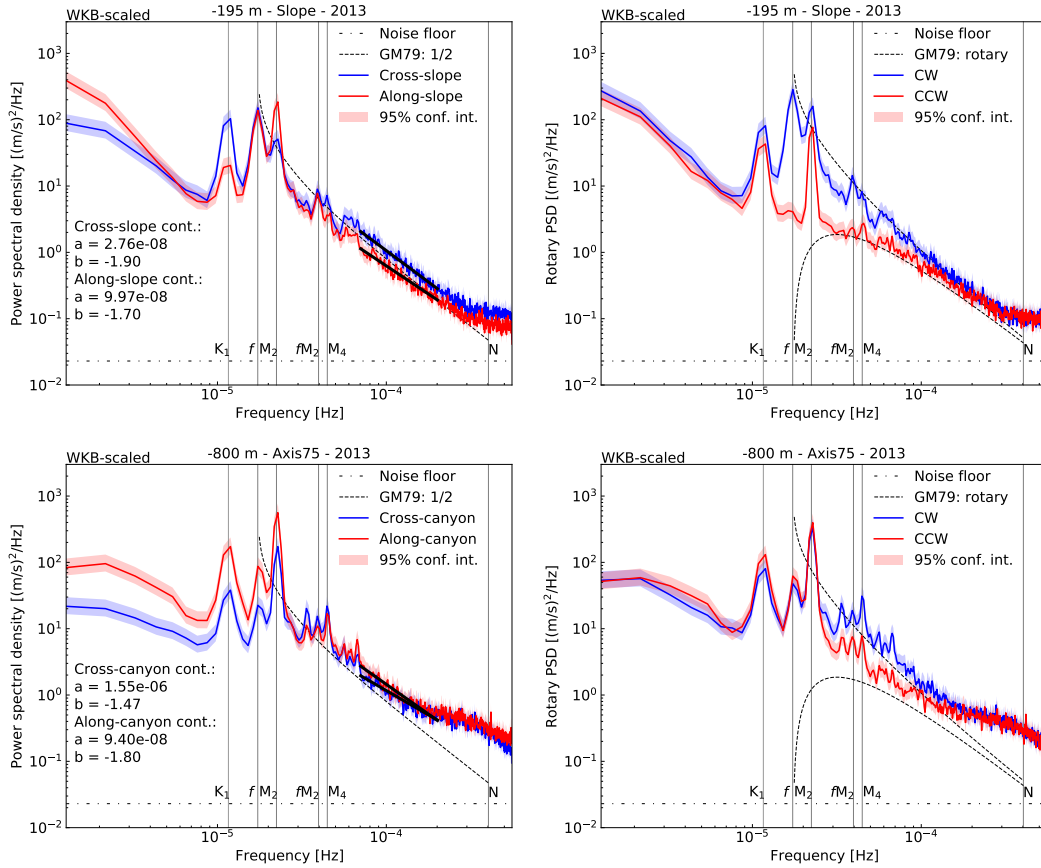


Figure 10: Mid-depth annual PSD (left) and rotary (right) spectra of adjusted (see Section 4) and WKB-scaled horizontal velocity data, for Slope (top) and Axis (bottom), in 2013. For PSD, both cross- (blue) and along-slope/canyon (red) components are shown; for rotary, both CW (blue) and CCW (red) components are shown. 95% confidence intervals are shaded. The instrument noise floors (dotted line) and primary frequency constituents with integration range (vertical lines and shading) are included. For PSD, fitted 'continuum' power-law amplitudes and slopes are for the imposed black lines, and the GM79 spectrum (1/2 amplitude) is the dashed line. For rotary, the GM79 spectrum is shown as rotary components (dashed lines, CW is upper). Spectra at both sites are characteristically red, with prominent tidal and near-inertial peaks. *Use finer resolution. Plot band ranges.*

Hz) forms the trailing end of the spectrum. The continuum was chosen to range between the M_4 spectral sum peak and the noise floor affected portion

of the Axis 55 kHz instrument.

At Slope, the mid-depth power spectra are similar to previous observations on the VICS (Thomson et al., 1990; Allen et al., 2001). Tidally, the semidiurnal peak is the strongest along-slope constituent (about 2×10^2 (m/s) 2 /Hz), while the diurnal peak is stronger cross-slope (about 1.5×10^2 (m/s) 2 /Hz). The near-inertial peak is of similar strength in both directions (about 1.5×10^2 (m/s) 2 /Hz). The sub-diurnal range is strongest along-slope, with strength increasing inversely to frequency. Above the minor sum-frequency peaks (fM_2 , M_4 , etc.), the continuum trails off slightly whiter than the expected GM slope of -2, mostly cross-slope, with effects from the noise floor becoming apparent near N (apparent in high frequency-resolution spectra). All frequency bands are strongest in the CW rotary component, particularly the near-inertial constituent, as expected for the northern hemisphere.

At Axis, the sub-diurnal, tidal, and near-inertial power trends toward along-canyon, rectilinear components, suggesting topographic guiding of flow even at mid-depth. Compared to Slope, the Axis sub-diurnal range is somewhat weaker at its low end, while the rest of the spectrum appears slightly more energetic, with a whiter continuum and notable high-frequency enhancement approaching N .

5.2 Depth dependence

At each site, there is directionally and rotationally variable adjustment of spectral power near-topography that is frequency-dependent. The WKB-scaled PSD and rotary spectra were time-averaged in an annual 2D depth-frequency analysis (Figure 11), and results show a general increase (or decrease for near-inertial at Slope) in spectral power (over an order of magnitude) in a concentrated layer (< a few hundred metres) above the bottom. Intensified near-slope layers are not uncommon, and are driven by focused incident internal wave energy that enhances up-slope flow (Polzin et al., 1997; Nash et al., 2004; Kunze et al., 2012). Similar results are evident back to a seminal study by Hotchkiss and Wunsch (1982) who found a $\sim 10\times$ increase in near-slope internal wave energy near Hudson Canyon, with a depth-dependent vertical scale of about 150 m AB at -400 m depth.

At Slope, the sub-diurnal, tidal, and continuum bands show near-slope intensification, while the near-inertial band shows attenuation of a similar magnitude, generally below -200 m depth (about 150 m AB). The sub-diurnal band shows intensification in mostly the along-slope and rectilinear rotary components. The diurnal band shows intensification in mostly the along-slope and CCW components, while the semidiurnal and continuum bands show inten-

sification that is fairly equally distributed directionally and mostly CW. The near-inertial band shows near-slope attenuation that is most evident in its CW component.

At Axis, most frequencies constituents display rectilinear, along-canyon near-bottom intensification, generally below -750 m depth (about 200 m AB). The sub-diurnal, diurnal, and near-inertial intensification is entirely along-canyon, with little to no power in the cross-canyon direction. The near-inertial band, in contrast to Slope, has bottom-intensified flow that is almost entirely along-canyon. The semidiurnal intensification is strongly along-canyon, but with a medium-strength cross-canyon signal that is sharply attenuated below about 100 m AB. Continuum intensification applies fairly equally across all components, both directional and rotary.

Qualitative analysis suggests that at Slope the near-bottom enhanced layer is most prominent up to about 150 m AB, and at Axis up to about 250 m AB. However, the sub-diurnal band shows enhancement of about an additional 50 m in the vertical, compared to all other constituents. A vertical scale analysis of the topography-enhanced bottom layer was performed for each site, and results generally agree with the general qualitative observations. Gemmrich and Klymak (2015) found that internal waves incident on sloped topography can induce a near-bottom turbulent flow layer, and that the vertical scale of the effect on incident mode-1 internal wave induced flow can be approximated as:

$$H \approx \frac{\pi U}{N} \quad (12)$$

where U is the forcing by cross-slope velocity. For moderate to strong velocities within 100 m AB and approximate buoyancy values for near-topography depths at Slope ($U \approx 0.15$ m/s; 3.5×10^{-3} rad/s at -350 m) and Axis ($U \approx 0.25$ m/s; 2×10^{-3} rad/s at -900 m), estimates result in vertical scales of about 135 m and 250 m, respectively. These estimates are similar to the qualitative observations, and agree with the results of Gemmrich and Klymak (2015) for enhanced bottom-layer flow with similar forcing and stratification; however, they do not account for the observed difference in sub-diurnal vertical scale, or increased stratification near topography (due to the climatology data being from a nearby open-ocean site). It is possible that the extended vertical scale of the sub-diurnal range could be due to its longer wavelengths at low-frequencies or the greater cumulative power of its broad bandwidth.

5.3 Frequency dependence and seasonality

There is frequency-dependent variability in the intensity and seasonality of the observed enhancement and attenuation. Spectral constituents were integrated

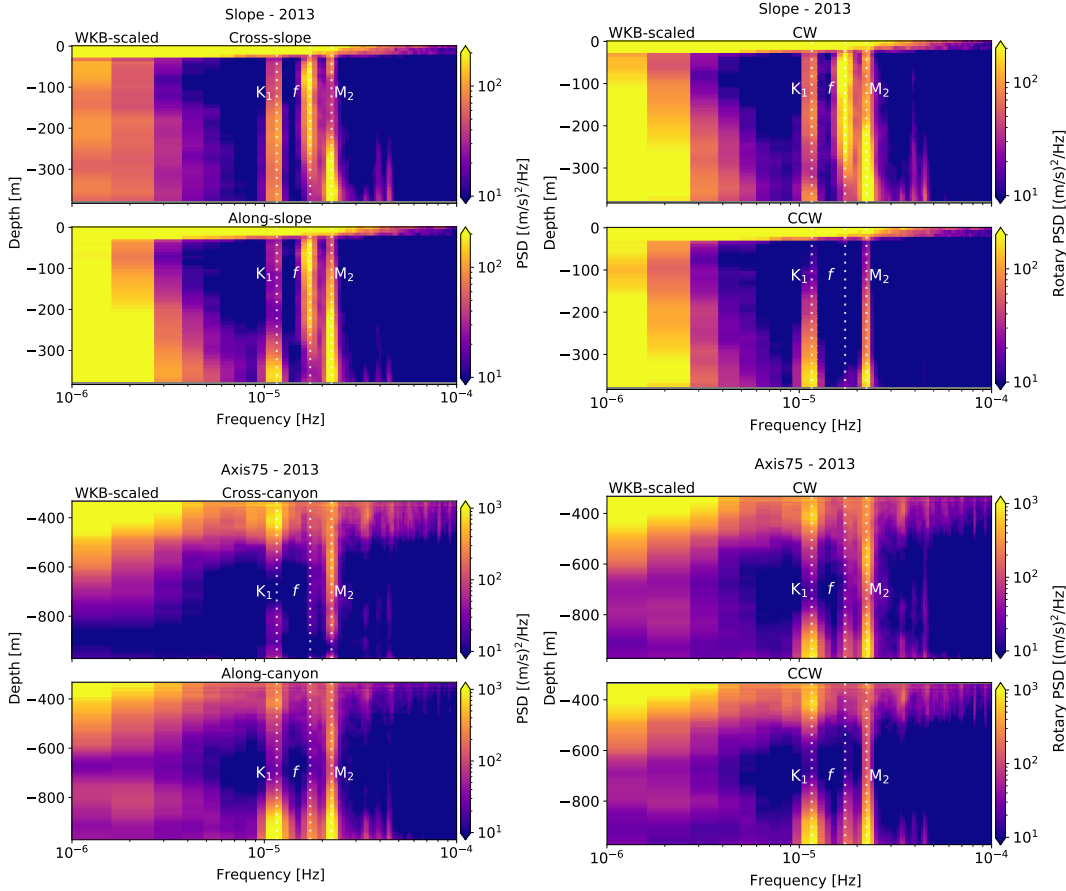


Figure 11: Depth-frequency PSD (left) and rotary (right) plots for Slope (top) and Axis (bottom), in 2013. For each site, components are separated as cross- (upper) and along-slope/canyon (lower). Spectra are from 'adjusted' and WKB-scaled horizontal velocity data. At both sites there is near-bottom intensification of individual frequency constituents (and near-bottom attenuation of the near-inertial band at Slope).

over bandwidths estimated to best comprise their peak or continuum (shown as shaded regions in Figure 10), at each depth bin, resulting in a 'depth-band power' analysis for each constituent, from both WKB-scaled PSD and rotary spectra. Plots for each site and constituent, in both PSD and rotary formats, are available in Appendix A (Section 7, Figures 21, 22, 23, and 24). Frequency ranges for analysis were chosen as sub-diurnal ($\leq 1.08 \times 10^{-5}$ Hz), diurnal ($1.08 - 1.30 \times 10^{-5}$ Hz), near-inertial ($1.52 - 1.95 \times 10^{-5}$ Hz), semidiurnal ($2.17 - 2.39 \times 10^{-5}$ Hz), and the continuum ($6.08 \times 10^{-5} - 1.00 \times 10^{-4}$ Hz).

5.3.1 Sub-diurnal

For the sub-diurnal range, the near-topography enhancement is approximately $1.5\times$ orders of magnitude at Slope, and $2\times$ orders of magnitude at Axis. At Slope, the enhancement layer is most prominent in the along-slope and CW components, while at Axis the enhancement is nearly entirely along-canyon and rectilinear. Propagation of incident or generated sub-diurnal internal waves should be restricted to near-topography flow, at this latitude, and this range may be contaminated by regional mean currents.

Sub-diurnal enhancement seasonality at Slope consists of pulses in both the fall and winter, and at Axis is mostly non-existent with only the occasional fall pulse evident. Potential forcing mechanisms for the observed sub-diurnal seasonality are not obvious; however, speculatively, regional low-frequency currents incident with topography or seasonal changes in stratification are likely contributors.

5.3.2 Diurnal

For the diurnal constituent, the near-topography enhancement is approximately $1.5\times$ orders of magnitude at Slope, and $2\times$ orders of magnitude at Axis. At Slope, the enhancement layer is most prominent in the along-slope and CCW components, while at Axis the enhancement is nearly entirely along-canyon and rectilinear. The diurnal constituent is sub-inertial at this latitude (as is the sub-diurnal range), and this result is similar to that of Cummins and Oey (1997), who found that sub-inertial diurnal internal tide generation was prevalent on the VICS adjacent continental slope, but that motions were evanescent (trapped) along-slope, unable to radiate offshore as they are restricted north of their turning latitude ($\sim 30^{\circ}\text{N}$, with results confirmed at similar Pacific slopes (Rudnick, 2015) and seamounts (Robertson et al., 2017).

Diurnal enhancement seasonality at Slope shows a regular pulse from late-spring (months 4/5) through summer and a weaker pulse in the fall/early-winter, while seasonality at Axis is not readily apparent. Cummins (2000) similarly associated strengthened diurnal tidal flow over the VICS with increased stratification in summer. Additionally, it is interesting that the timing of the late-spring/summer pulse aligns well with the sharp annual transition to upwelling-favourable equatorward mean currents at Slope, a prominent regional physical process (Crawford and Thomson, 1984).

Diurnal barotropic spring-neap forcing is consistently close to in-phase, with generally minor phase-lag correlations and a scaled depth-mean of similar amplitude, at both sites (Figure 12). 4-month phase lag correlations were performed between the band-passed depth-mean power and nearby surface level

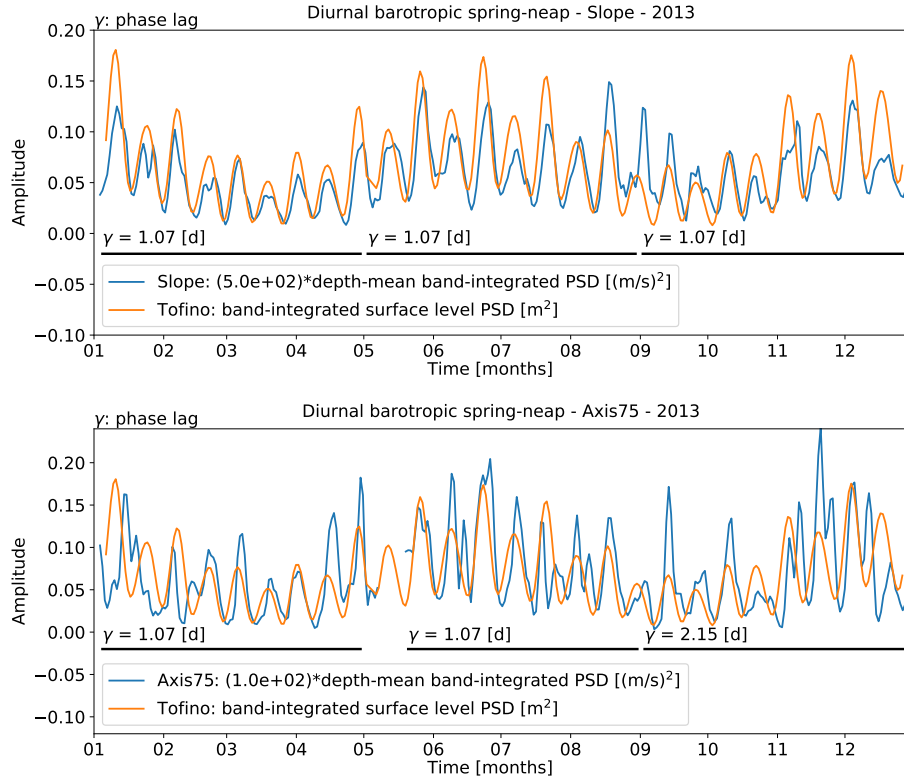


Figure 12: Diurnal barotropic forcing comparison. Phase and scaled amplitude comparisons for band-integrated power of the diurnal surface levels (Tofino, orange) and WKB-scaled depth-mean diurnal power (blue) at Slope (top) and Axis (bottom), in 2013. Phase-lag correlations are listed for four-month intervals. There is a consistently minor phase lag of about a day that may actually be null, considering uncertainties.

time series, in segments of months 1-4, 5-8, and 9-12. Surface-level data were obtained from the Canadian Hydrographic Service (CHS) operated gauge in Tofino, approximately 90 km due north of Barkley Canyon, as time series of deviation from chart datum. The surface level power spectra were band-pass filtered with the same parameters as the depth-band spectra, to compare phase. Results are generally minor, with phase-lag correlation consistently about 1 day, less than the time-resolution of the spectral estimates. Furthermore, as the diurnal frequency is sub-inertial, it is unlikely for there to be remote baroclinic forcing. Speculatively, if a lag of 1 day was present, this would suggest a baroclinic generation site within 200 km, based on a K1 mode-1 wave speed of about 2 m/s (Crawford and Thomson, 1984). A likely candidate would be

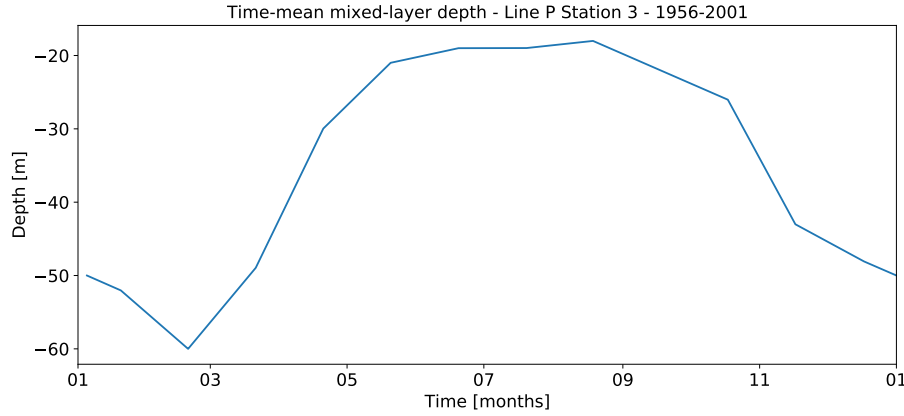


Figure 13: Seasonal mixed-layer depth. Monthly-averaged mixed-layer depth for Line P station 3, as determined by Li et al. (2005). Variability in mixed-layer depth effects near-inertial input from wind.

diurnal shelf waves generated near the mouth of the Strait of Juan de Fuca (about 100 km east), which are able to propagate poleward along the VICS (Crawford and Thomson, 1984), unlike diurnal internal tides at this latitude. However, there is enough uncertainty in the comparisons that the phase lag could effectively always be null, suggesting that the diurnal band is primarily forced by the local barotropic diurnal tide.

5.3.3 Near-inertial

For the near-inertial constituent, the near-topography attenuation at Slope is approximately $1.5 \times$ orders of magnitude at Slope, and the enhancement at Axis about $2 \times$ orders of magnitude. At Slope, the near-inertial power above the attenuation region is evenly distributed directionally and entirely CW down to about 150 m AB, while at Axis the enhancement layer is nearly entirely along-canyon and rectilinear up to about 200 m AB. Thomson et al. (1990) found that as near-inertial internal waves approach a slope they become increasingly attenuated as they are absorbed by increased vertical shear in the background flow, associated with topographically trapped oscillations. It is possible that the near-topography attenuation on the upper-slope could limit the ability of near-inertial waves to propagate into the canyon; hence only the strongest fall and early-winter pulses showing up at Axis. If this is the case, it is curious to see consistent bottom-intensified near-inertial flow in the canyon, potential forcing for which could be from near-inertial flow across the open mouth of the canyon, where attenuation may be reduced.

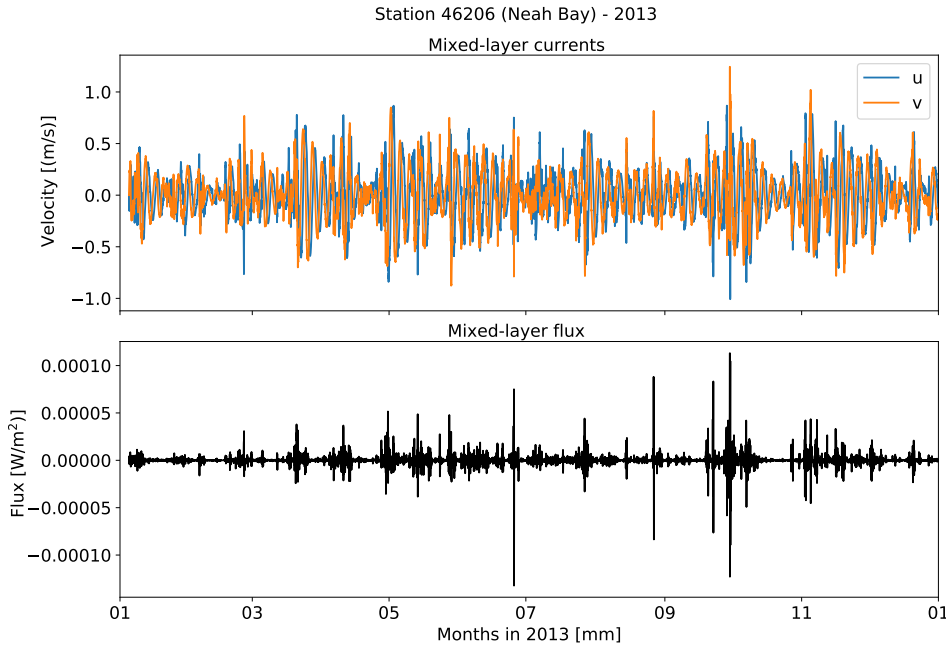


Figure 14: Induced mixed-layer currents and flux, for Station 46206 in 2013, as determined from a slab model analysis. *These should be near-inertial band-passed!*

At Slope, near-inertial seasonality above the attenuation region is highly intermittent and most evident in the fall and early-winter, with notable pulses potentially occurring year round, while at Axis only the significant fall and early-winter events from Slope are evident within the canyon. This is likely due to the intermittent nature of the regional wind events forcing the near-inertial internal waves; it is typically only small cold fronts and lows with considerable CW rotation that act as significant sources of near-inertial flux, occurring most often in the fall and early-winter and typically inducing greater inertial currents than even synoptic scale storms (D'Asaro, 1985; Alford, 2001; Voelker, 2020).

As such, it appears that near-inertial forcing is qualitatively linked with the timing of regional wind events in the fall and early-winter. Wind data were obtained from the closest Fisheries and Oceans Canada (DFO) weather buoy, La Perouse (46206), approximately 50 km north of Barkley Canyon, as time series of magnitude and direction for each comparison year. A slab model analysis was conducted as by D'Asaro (1985) and Alford (2001), who suggest that

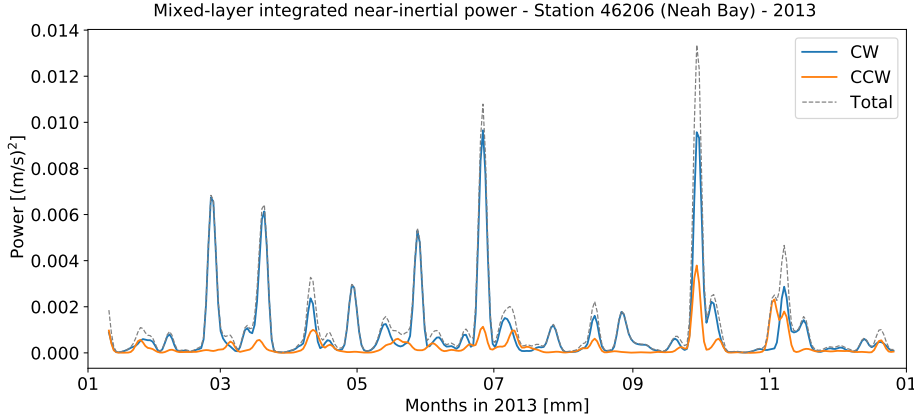


Figure 15: Mixed-layer integrated near-inertial forcing comparison, for band-integrated Station 46206 slab power and depth-mean power at Slope, in 2013. Though there is little statistical correlation between the wind and near-inertial seasonality, there is a qualitative link in the timing of contributing wind events in the fall and early-winter. *Add depth-mean Slope time series.*

specific wind events can induce near-inertial currents in the seasonally variable mixed-layer, where a divergent 'pumping' mechanism at its base (Voelker, 2020) 'strums' stratification-dependent vertical modes, exciting near-inertial internal waves in the waters beneath (Alford et al., 2012). From the wind time series data, wind stress is calculated as in Garratt (1977), as:

$$\tau_0 = \rho C_D V(z)^2 \quad (13)$$

where ρ is the density of air approximated as 1, $V(z)$ is the complex wind velocity vector, and C_D is the characteristic drag coefficient determined by:

$$C_D \times 10^3 = 0.51V^{0.46} \quad (14)$$

For appropriate seasonality, a mixed-layer of seasonally varying depth H must be considered, and is defined for the nearby (35 km) Line P station 3 as in Thomson and Fine (2003) and Li et al. (2005) (Figure 13). Assuming a null initialisation parameter u_{I1} at time t_1 , wind generated slab layer currents at time t_2 are then computed as:

$$u_{I2} = u_{I1}e^{-\omega\Delta t} - \frac{T_t}{H\omega^2}(1 - e^{-\omega\Delta t}) \quad (15)$$

where a damped rotation frequency, ω , is determined as:

$$\omega = r + if \quad (16)$$

with $r = 0.15f$ as an artificial damping parameter, as defined in Alford (2001); and

$$T_t = \frac{\Delta T}{\Delta t} \quad (17)$$

is related to the complex stress vector defined as:

$$T = \frac{\tau_x + i\tau_y}{\rho_{ML}} \quad (18)$$

where $\rho_{ML} = 1024 \text{ kg/m}^3$ is the average density of the mixed-layer. The near-inertial flux by the wind into the mixed layer at time t_2 is then computed as:

$$\Pi = \text{Re} \left\{ \frac{T_t^*}{\Delta t |\omega|^2 H} \left[\left(u_{I1} + \frac{T_t}{\omega^2 H} \right) (e^{-\omega \Delta t} - 1) + \frac{T_t}{\omega H} \Delta t \right] \right\} \quad (19)$$

Finally, the slab currents are band-passed and, along with the seasonal depth of the mixed-layer, multiplied with stratification-dependent vertical modes as determined from the solutions of the...

MOVE UP. Slab model results show significant mixed-layer currents (up to X m/s) and positive flux (up to X) associated with notable wind events (Figure 14). However, not every wind event appears to contribute equally to near-inertial slab layer currents, with the largest inputs in the fall and early-winter, and some other events barely contributing at all. Near-inertial wind contributions to the slab layer are not statistically correlated with internal wave observations, but the qualitative timing of the fall and early-winter events appears to be associated (Figure 15). Finally, the vertical mode decomposition suggests that the induced near-inertial slab currents 'strum' different modes depending on the timing of wind events and the seasonal mixed-layer depth...

(Near-inertial vertical modes plot.)

MOVE UP. These results suggest that the seasonality of the near-inertial forcing is dependent on many factors, possibly contributing to the observed intermittent behaviour. Wind events must meet specific requirements in size, direction, rotation, and speed, to best contribute energy into the mixed-layer, as discussed (Alford, 2001). The mixed-layer itself is seasonally variable, and its depth is crucial to both receiving and transmitting energy into the internal wave field, below; regional mixed-layer seasonality shifts the near-inertial input peak towards October, when the mixed layer is thin and storms are prevalent (Thomson and Fine, 2003; Li et al., 2004). The induced near-inertial mixed-layer currents then 'strum' different vertical modes dependent on the seasonal mixed-layer depth (Alford et al., 2012). Cumulatively, if wind events are the

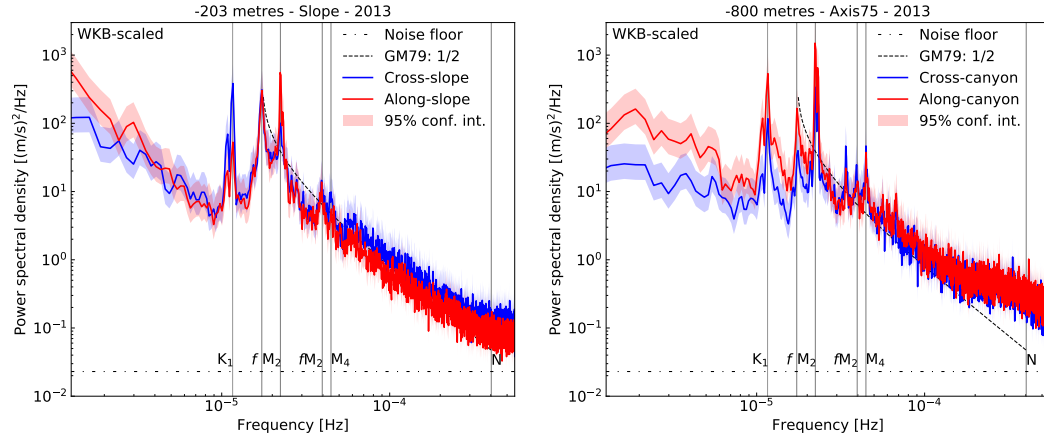


Figure 16: High frequency-resolution PSD of WKB-scaled horizontal velocity data, -203 m at Slope (left) and -800 m at Axis (right), in 2013. Even with higher frequency-resolution, there are no additional peaks or apparent blue-shift on the near-inertial constituent, suggesting regional forcing. *Zoom f.*

primary near-inertial forcing, these factors would all contribute to a highly intermittent near-inertial internal wave field, as observed.

Additionally, as free near-inertial internal waves are generated at the surface mixed-layer and must propagate downward (CW) and equatorward due to the effects of turning latitudes, there is often a blue-shift associated with remote near-inertial forcing (Garratt, 1977; Voelker et al., 2020). However, high frequency-resolution spectra (Figure X) do not resolve any additional near-inertial peaks, and the primary peak is situated at the local inertial frequency (f), suggesting that most of the forcing is regional.

5.3.4 Semidiurnal

For the semidiurnal constituent, the near-topography enhancement is approximately $2\times$ orders of magnitude at Slope, and $3\times$ orders of magnitude at Axis. At Slope, the enhancement layer is evenly distributed directionally and entirely CW up to about 150 m AB, while at Axis the enhancement is nearly entirely along-canyon and rectilinear up to about 200 m AB. Locally, Drakopoulos and Marsden (1993) found that for the Vancouver Island continental margin, seaward of the shelf break (as at Slope), that the semidiurnal internal tide propagation was strongly CW downward, with this result noted at other slopes (Subeesh et al., 2021). There is also evidence of near-bottom elevated energy-flux associated with both semidiurnal internal tide generation and incident reflection on continental-slopes, with location dependent vertical scales

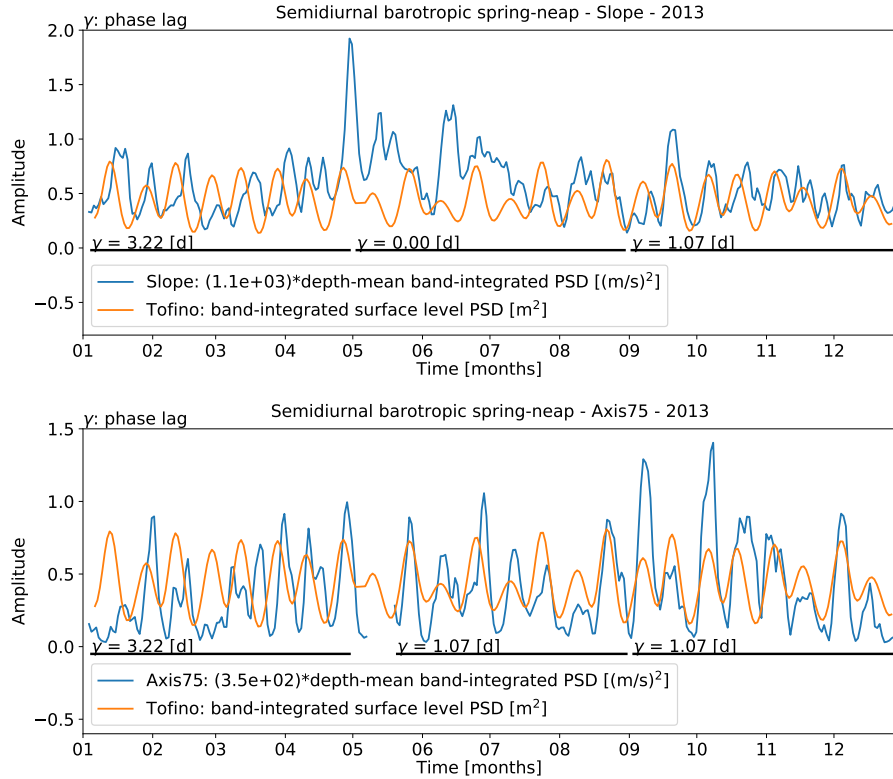


Figure 17: Semidiurnal barotropic forcing comparison. Phase and scaled amplitude comparisons for band-passed power of the semidiurnal surface levels (Tofino, orange) and WKB-scaled depth-mean band-integrated diurnal power (blue) at Slope (top) and Axis (bottom), in 2013. Phase-lag correlations are listed for four-month intervals. Though the instrument time series is highly irregular, there is an intermittent phase lag of up to 3-4 days that suggests a mix of local barotropic and remote baroclinic forcing.

all within a few hundred metres AB (Terker et al., 2014; Xie and Chen, 2021). Further studies have shown that where criticality (β/α , as detailed in section 3) is near to 1, also typically below the shelf-break, incident semidiurnal internal tides are most strongly subject to near-slope enhancement (Robertson et al., 2017).

The Slope and Axis mooring sites are supercritical and subcritical to incident semidiurnal internal tides, respectively. Critical slope regions were determined from the gradient of bathymetry data obtained from the National Oceanic and Atmospheric Administration (NOAA) National Centre for Environmental

Information, as 3 arc-second resolution mean sea level depth, for the Barkley Canyon region (Figure 5). At the Slope site, the local slope is $\beta \approx 0.060$, supercritical to the semidiurnal propagation angle $\alpha_{M2} \approx 0.026$ at that depth, and a criticality of 2.3 (Figure 7). This suggests that there will be some focusing of incident semidiurnal energy near topography, with some reflected CW downward and seaward in this region, as observed. The Slope site in particular sits adjacent to a large near-critical region below the shelf-break (Figure 5), a potential source of observed downward semidiurnal energy. For the Axis site on the canyon floor, the local slope angle is $\beta \approx 0.019 < \alpha_{M2} \approx 0.036$, a criticality of 0.53 (Figure 7). As such, this portion of the canyon floor is subcritical to the freely propagating semidiurnal internal tides, suggesting upward reflection. However, as the canyon walls are generally supercritical, and the surrounding floor is near-critical (Figure 5), the propagation of both locally generated and incident semidiurnal internal tides near the Axis site is likely complex, potentially contributing to a highly 'channeled' deep-canyon semidiurnal flow, as observed.

Semidiurnal enhancement seasonality at Slope is similar to the diurnal, showing a regular pulse that begins in the late-spring/early-summer (months 4/5) and a weaker pulse in the fall/early-winter, while seasonality at Axis is not readily apparent. Drakopoulos and Marsden (1993) similarly found that the semidiurnal internal tide field on the continental margin off of Vancouver Island gained strength in the late-spring through summer, and attenuated by September, associated with seasonal changes in stratification.

Semidiurnal barotropic spring-neap forcing is in-and-out of phase at both sites, suggesting a combination of local barotropic and remote baroclinic forcing (Figure 17). Furthermore, scaled depth-mean time series amplitudes vary greatly from those of the barotropic surface tide and by comparison are quite irregular. Phase lag is intermittent throughout the year, with some inter-annual variability, and averages up to 3-4 days when present. Regional mode-1 M2 phase speed, c_1 , averages about 3.0 m/s, with minimal seasonal variation below the mixed layer (Zhao et al., 2016). For the average phase offset of 3-4 days, this suggests a travel distance of 700-1000 km. At this distance, a likely generation site for the baroclinic remote forcing is the Mendocino Escarpment that runs E-W off the coast of North California, one of the strongest generation sites for mode-1 and mode-2 semidiurnal internal tides in the northeast Pacific (Althaus et al., 2003; Arbic et al., 2012; Zhao, 2017; Morozov, 2018). Strong northward propagating mode-1 M2 internal tides, along with the escarpment's location about 800 km to the south of Barkley Canyon (3.5 days), agree well with the observed intermittent phase lag.

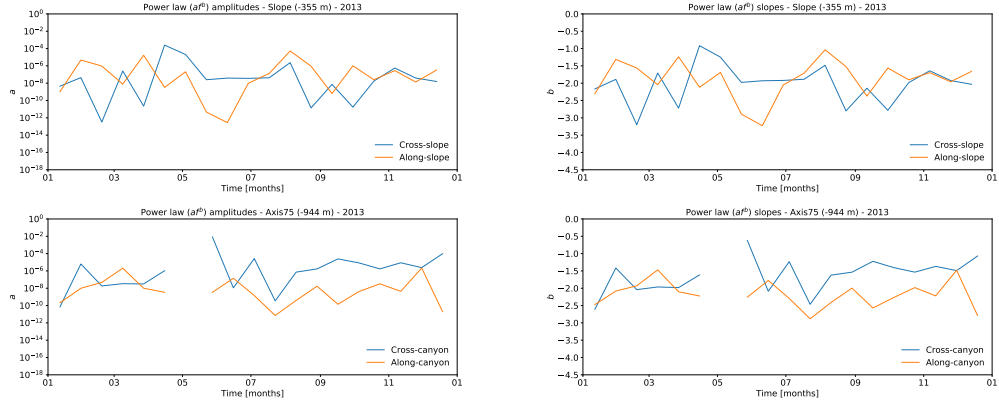


Figure 18: Time series of a and b power law fits. Amplitudes, a (left), and slopes, b (right), of power law (af^b) fits to WKB-scaled near-bottom continuum PSD at Slope (top) and Axis (bottom), in 2013. Compared to GM, amplitudes are heightened and slopes are whitened. *Update and add GM lines.*

5.3.5 Continuum

For the high-frequency internal wave continuum, the near-topography enhancement is approximately $1\times$ orders of magnitude at Slope, and $1.5\times$ orders of magnitude at Axis. At Slope, the enhancement layer is mostly cross-slope and CW up to about 150 m AB, while at Axis the enhancement is evenly distributed directionally and mostly CW up to about 200 m AB. *Comparisons and speculation.*

Near-bottom, the slope of the continuum tends to be somewhat amplified and whitened as compared to the component-wise $1/2$ GM spectrum (Figure 18). For each component-wise time-step of the high frequency-resolution WKB-scaled PSD estimates (2048 point Hanning window, with 50% overlap) a power law of af^b was fit to the continuum range, resulting in a time series of a and b values. At Slope (-355 m), a values are consistently somewhat greater than GM, ranging from X to X, and b slope values are consistently somewhat whiter than GM, ranging from X to X, in mostly the X-slope direction. At Axis (-944 m), a values are consistently greater than GM and Slope, ranging from X to X, and b slope values are consistently whiter than GM and Slope, ranging from X to X. *Comparisons? GM level for a ?*

Continuum seasonality of enhancement at Slope is consistently similar to elements of the diurnal and semidiurnal bands, with the most notable feature being an obvious pulse in the late-spring that lasts through summer. Continuum seasonality at Axis is less apparent but most similar to elements of the

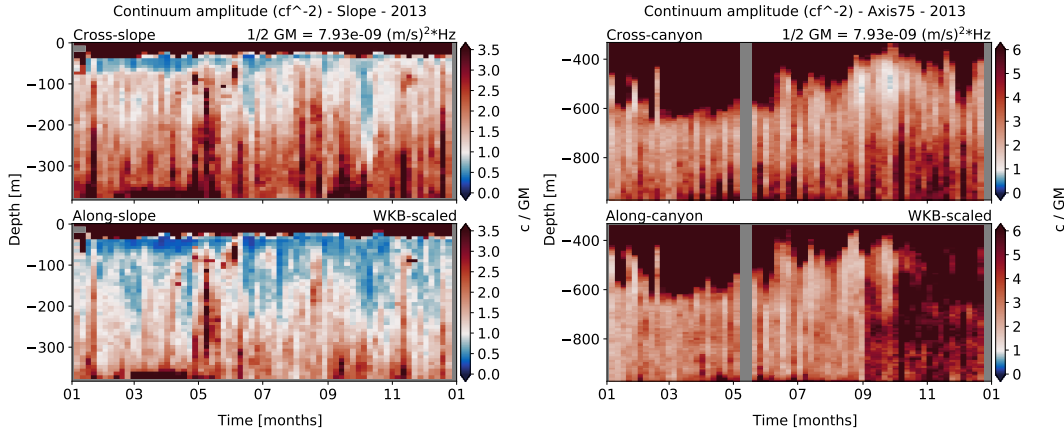


Figure 19: Continuum amplitude (c) versus GM amplitude over the same frequency range, for Slope (left) and Axis (right) in 2013. Results are obtained from WKB scaled spectra. Continuum component amplitudes are divided by the $1/2$ GM amplitudes determined using the same method to show elevated (red) and reduced (blue) internal wave energy through depth and time. Internal wave energy is generally enhanced near topography, as compared to the open-ocean.

near-inertial band, particularly in the fall. This suggests a potential cascade of energy from low-frequency constituents to high-frequency dissipative processes in the continuum range, driven tidally at Slope and by near-inertial internal waves at Axis. *Comparisons before speculation...*

Continuum amplitudes show a heightened state near topography, as compared to GM (Figure 19). Each power bin of the WKB-scaled continuum band was 'whitened' - multiplied by its corresponding frequency squared - and the band average value determined for c from a power-law fit of cf^{-2} . This was compared at each time-step and depth-bin against a value for the $1/2$ GM continuum over the same range, of $c_{GM} = 7.93 \times 10^{-9}(\text{m/s})^2\text{Hz}$, determined by the same method. The results reinforce the suggested cascading energy process, and show c amplitudes exceeding $3.5 \times \text{GM}$ at Slope, and $6 \times \text{GM}$ at Axis, at times and depths coinciding with observed continuum pulses. The differences in near-topography continuum amplitude components suggest that it is characteristically unlike the open-ocean GM spectrum. *Comparisons and speculation.*

Dissipation rates, ε , are elevated near topography at both sites (Figure 20). As derived from internal wave interaction theory (Althaus et al., 2003), dissipation

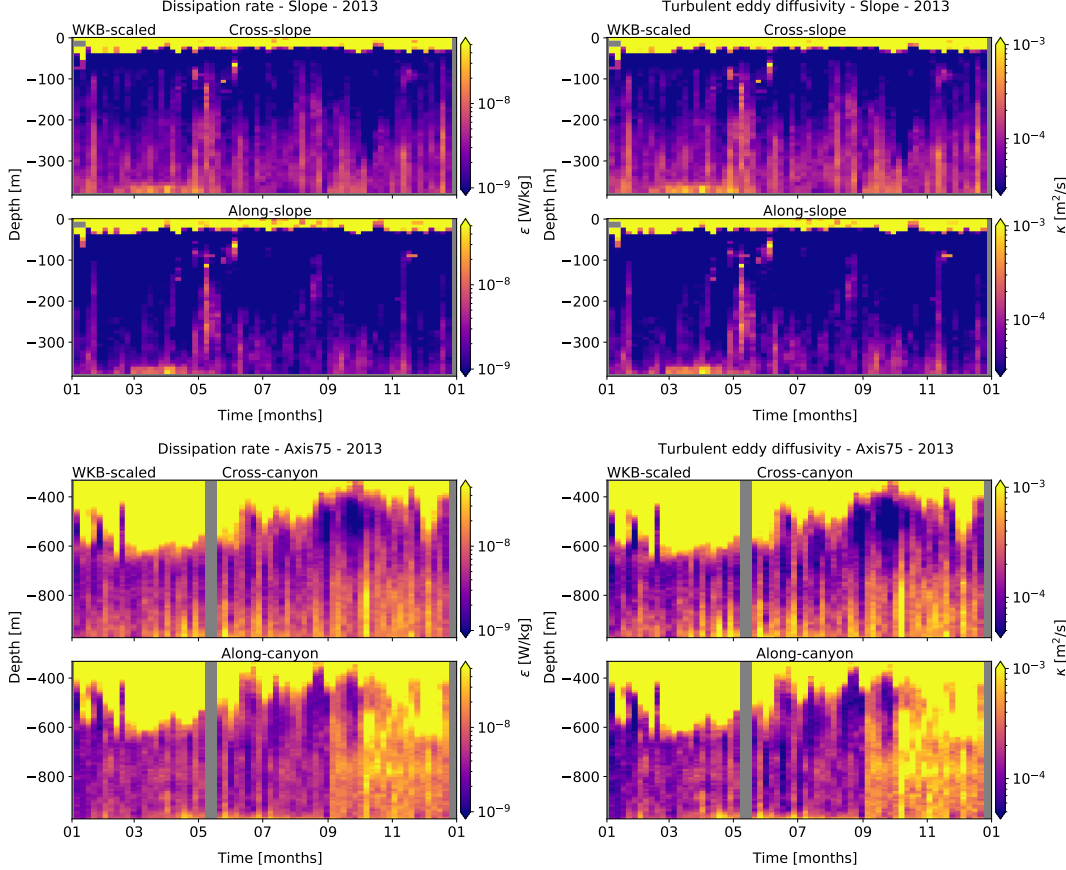


Figure 20: Dissipation (left) and diffusivities (right), for WKB-scaled horizontal velocity spectra at Slope (top) and Axis (bottom), in 2013. Both dissipation and diffusivities are heightened near topography.

estimates were calculated from the WKB-scaled c amplitude fits, as:

$$\varepsilon = \varepsilon_0 \frac{N^2}{N_0^2} \frac{\langle V_z^2 \rangle^2}{\langle GM V_z^2 \rangle^2} f(R_\omega) \quad (20)$$

where $\varepsilon_0 = 4.1 \times 10^{-11}$ W/kg, $N_0 = 5.24 \times 10^{-3}$ rad/s is the GM reference buoyancy frequency, $N = 2.53 \times 10^{-3}$ rad/s is the local reference buoyancy frequency used for WKB scaling, $\langle V_z^2 \rangle^2 / \langle GM V_z^2 \rangle^2$ is the measured shear/strain ratio of continuum energy versus GM energy over the same bandwidth, and the upper bound:

$$f(R_\omega) = \left(\frac{R_\omega + 1}{R_\omega} \right)^2 \left[\text{arc cosh} \left(\frac{N}{f} \right) + \frac{25 \text{arc cos}(f/N)}{\sqrt{R_\omega}} \right] \quad (21)$$

is as from Sun and Kunze (1999), with $R_\omega = 2.13$ being the semidiurnal shear/strain ratio as used by Kunze et al. (2002). Results are consistent with those found in other slope and canyon regions (Kunze et al., 2002), exceeding 10^{-8} W/kg near the slope, and reaching 10^{-7} W/kg in the canyon depths.

More comparisons? Speculation.

Turbulent eddy diffusivities are also elevated near topography (Figure 20). Diffusivity is evaluated from dissipation estimates as in Kunze et al. (2002):

$$\kappa = \frac{\gamma \varepsilon}{N^2} \quad (22)$$

where $\gamma = 0.2$ is the mixing efficiency for high-Reynolds-number turbulence. Turbulent eddy diffusivities are again similar to findings at other slope and canyon sites, with slope diffusivities exceeding 10^{-3} m²/s near topography, and approaching 10^{-2} m²/s in the deep canyon (Kunze et al., 2002). Elsewhere, values are less than 10^{-5} , consistent with values found in open-ocean regions (Kunze et al., 2002). *More comparisons? Speculation.*

(Diffusivity plots)

6 Summary and conclusions

It was found that there is significant influence from topography on the local internal wave field at both sites, guiding flow and causing frequency-dependent focusing (sub-diurnal, tides, and continuum) or attenuation (near-inertial at Slope) of spectral power, generally up to $1.5\times$ orders of magnitude 150 m AB at Slope, and up to $2\times$ orders of magnitude 250 m AB at Axis. This near-topography enhancement has unique seasonality for individual frequency constituents that varies little inter-annually. Sub-diurnal and diurnal flows are sub-inertially trapped along topography and appear to be forced locally (barotropically), while free semidiurnal internal tides are focused and reflected near critical topography and appear to experience both local and remote (baroclinic) forcing. The near-inertial band is attenuated near the slope, and enhanced near the canyon bottom, with intermittent forcing that appears linked to regional wind events. Finally, the state of the internal wave continuum is elevated as compared to the open-ocean GM spectrum (over $3\times$ GM on the slope, and $5\times$ GM in the canyon), with enhanced dissipation (exceeding 10^{-8} W/kg near the slope, and 10^{-7} W/kg in the canyon) and diffusivity (exceeding 10^{-3} m²/s near the slope, and 10^{-2} m²/s in the canyon) near topography, and seasonality suggesting a cascade of energy from low-frequency constituents (tidal on the slope, and near-inertial in the canyon) to high-frequency dissipative processes.

Unfortunately, the WKB-stretch scaling applied throughout much of the analysis is based on deep CTD casts that were made nearby (21 km SE), but away from topography; the stratification profile captures the surface mixed-layer and pycnocline, but does not adjust for possible buoyancy effects near the slope or in the canyon (Figure 8). Hotchkiss and Wunsch (1982) noted increased stratification near areas of high 'topographic relief', such as the shelf-break and slopes. These highly stratified turbulent layers experience the effects of reflection, scattering, and internal tide and lee-wave generation, as well as amplification of internal waves and tides, in general. To properly mitigate the effects of depth dependent stratification variability, further research would benefit from site specific climatology data.

Results could be improved through increased sampling consistency between instruments (there were adjustments and instrument swaps through the sample years), and additional instruments (along the canyon and directly at the canyon rim) and overlapping comparison years between sites. Broader temporal and spatial coverage could provide insight into potential long-term decadal seasonality, along-canyon and vertical evolution of internal wave propagation such as reflection or breaking events, help to identify forcing for the low-frequency sub-diurnal range and the presence of bottom-enhanced near-inertial flow in the canyon, and potentially observe the long-term effects of changing climate on local water properties and processes.

Barkley Canyon is a dynamic submarine canyon and slope region with physical processes that show unique spatial and temporal characteristics. As canyons and slopes are known to contribute significantly to local productivity and even large-scale climate effects, ONC's Neptune cabled observatory is an exciting network for uncovering the science of the Vancouver Island continental margin and shelf. The accessibility of publicly available data for this region set Barkley Canyon as a key observational laboratory for furthering ocean research, fostering collaboration and communication between members of the amateur and professional scientific communities, both regionally and globally.

7 Appendix A: Frequency band comparisons

Incomplete

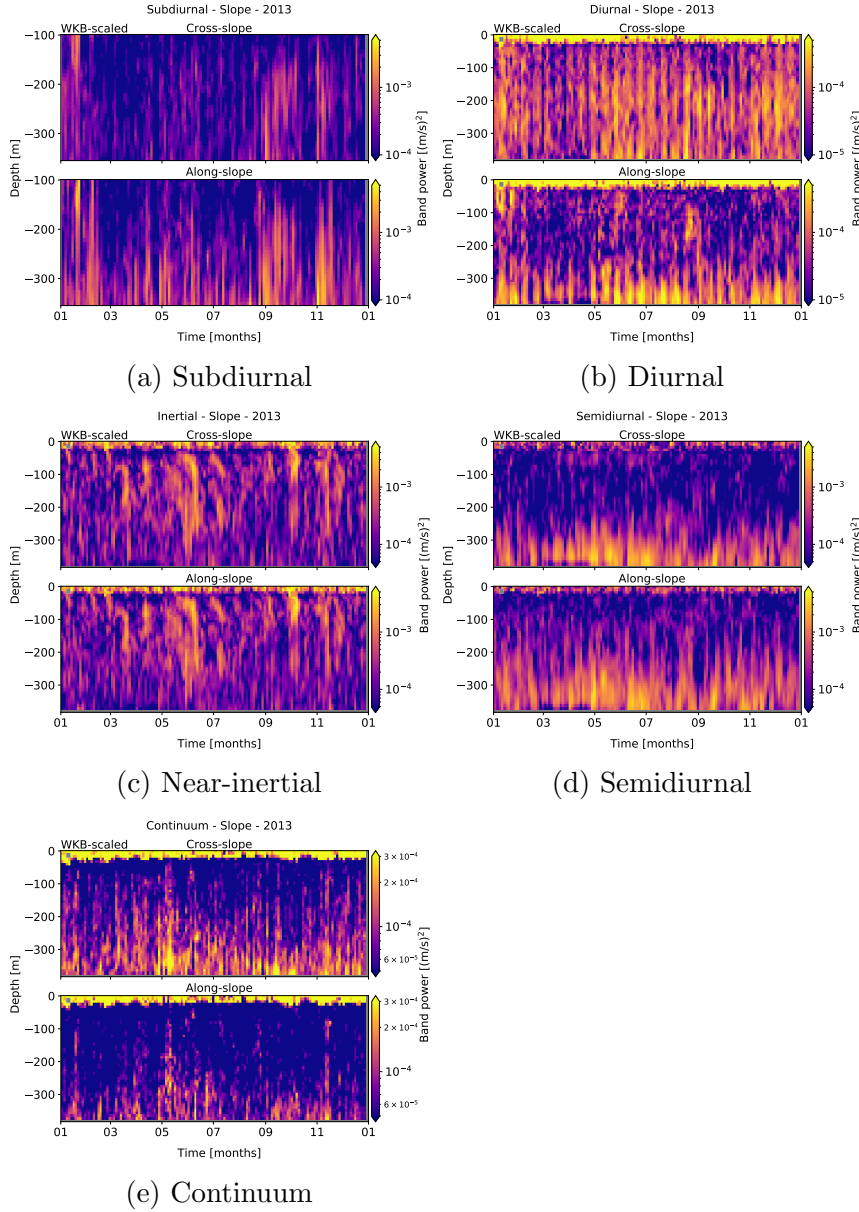


Figure 21: Band-intergrated PSD data for Upper Slope in 2013, for rotated, cleaned, and WKB-scaled horizontal velocity data. For each sub-figure, there are cross- (top) and along-slope (bottom) components. Intensity scales are adjusted for visual clarity of effects.

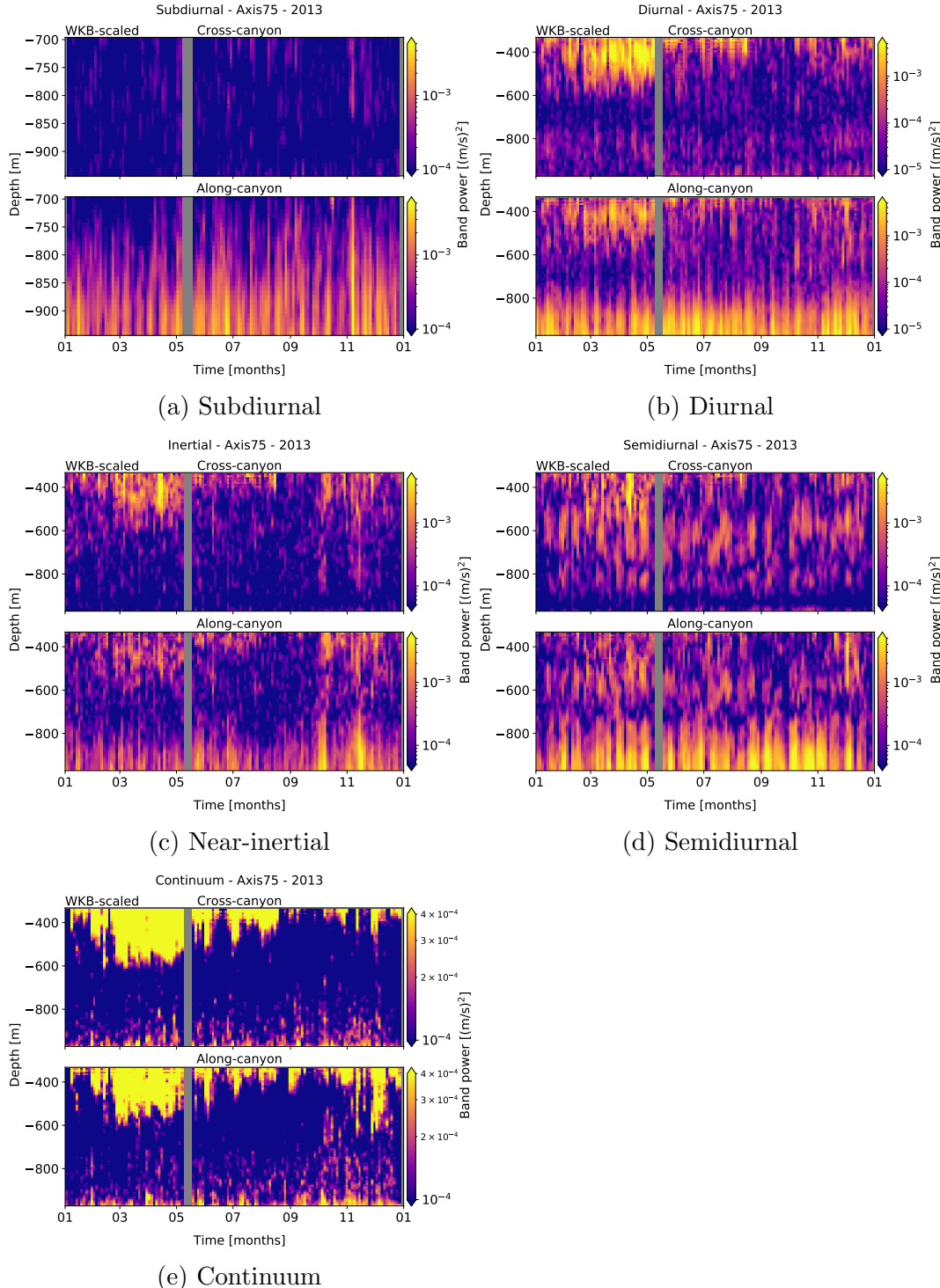


Figure 22: Band-integrated PSD data for Axis in 2013, for rotated, cleaned, and WKB-scaled horizontal velocity data. For each sub-figure, there are cross- (top) and along-slope (bottom) components. Intensity scales are adjusted for visual clarity of effects.

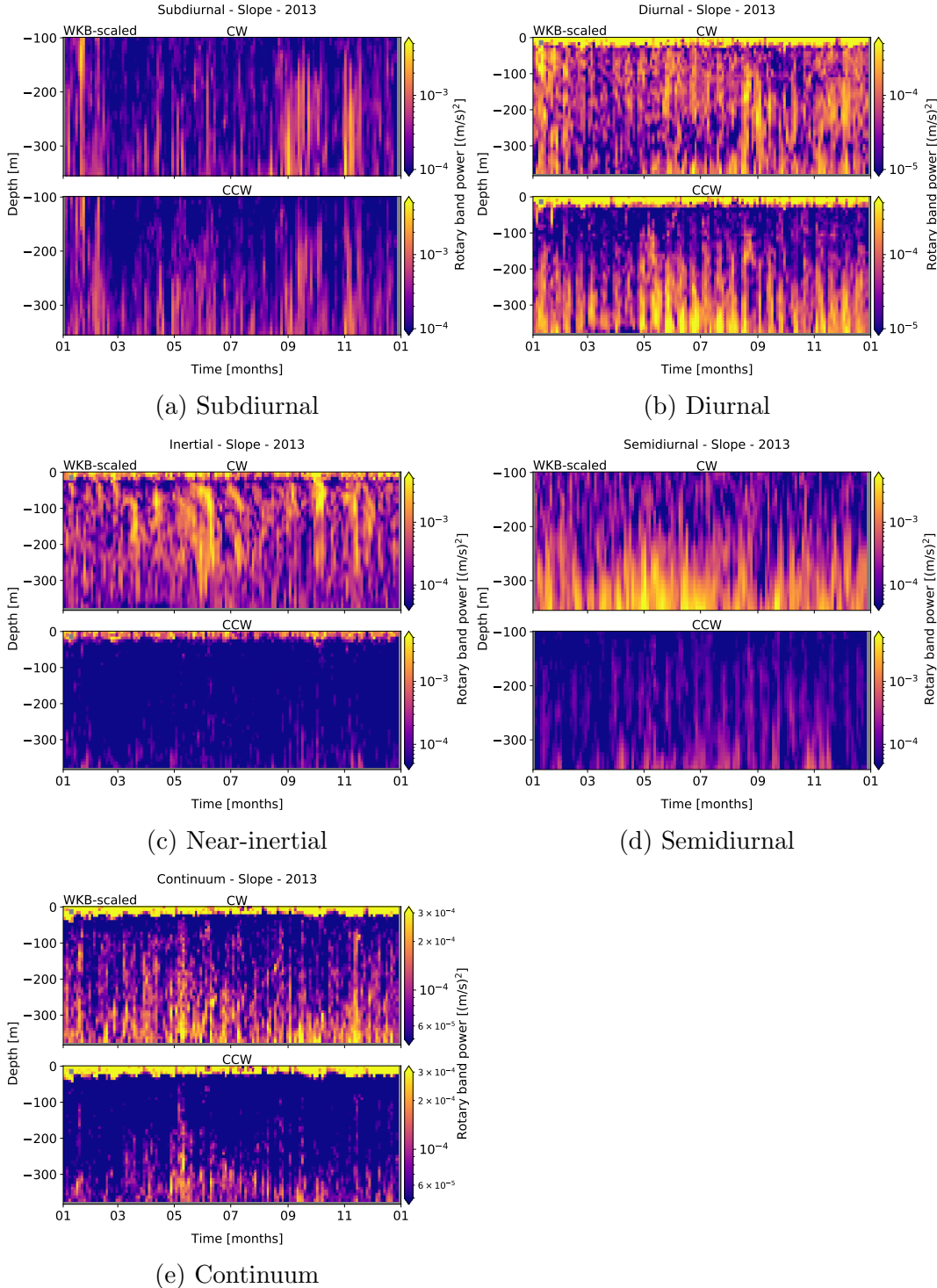


Figure 23: Band-integrated rotary data for Upper Slope in 2013, for rotated, cleaned, and WKB-scaled horizontal velocity data. For each sub-figure, there are CW (top) and CCW (bottom) components. Intensity scales are adjusted for visual clarity of effects.

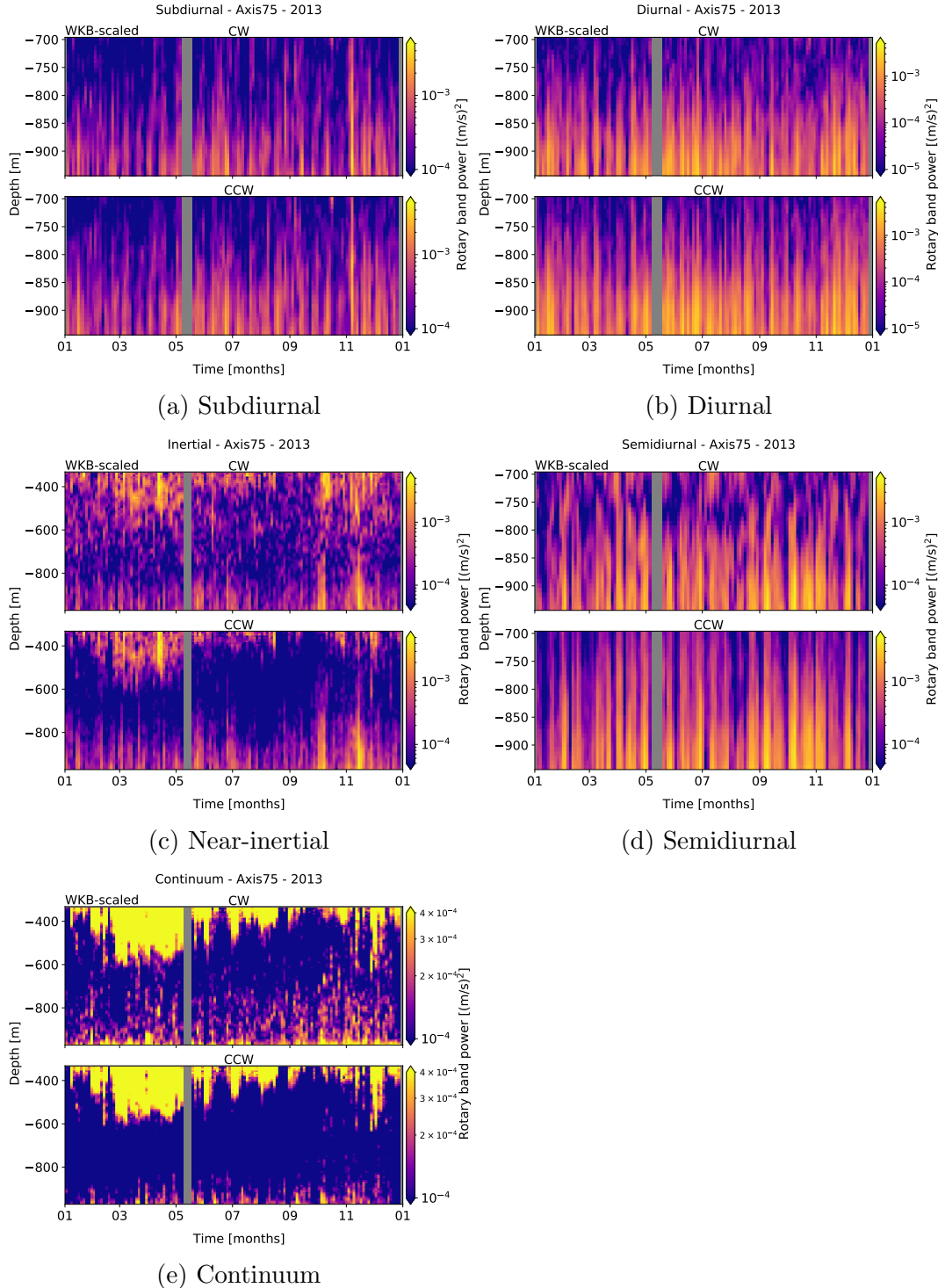


Figure 24: Band-integrated rotary data for Axis in 2013, for rotated, cleaned, and WKB-scaled horizontal velocity data. For each sub-figure, there are CW (top) and CCW (bottom) components. Intensity scales are adjusted for visual clarity of effects.

8 References

Incomplete

- Alford, M. H., MacKinnon, J. A., Zhao, Z., Pinkel, R., Klymak, J., & Peacock, T. (2007). Internal waves across the Pacific. *Geophysical Research Letters*, 34(24), 24601. <https://doi.org/10.1029/2007GL031566>
- Alford, M. H., Cronin, M. F., & Klymak, J. M. (2012). Annual cycle and depth penetration of wind-generated near-inertial internal waves at ocean station papa in the northeast pacific. *Journal of Physical Oceanography*, 42(6), 889–909. <https://doi.org/10.1175/JPO-D-11-092.1>
- Allen, S. E., Vindedirinho, C., Thomson, R. E., Foreman, M. G. G., & Mackas, D. L. (2001). Physical and biological processes over a submarine canyon during an upwelling event. *Canadian Journal of Fisheries and Aquatic Sciences*, 58(4), 671–684. <https://doi.org/10.1139/f01-008>
- Carter, G. S., & Gregg, M. C. (2002). Intense, variable mixing near the head of Monterey Submarine Canyon. In *Journal of Physical Oceanography* (Vol. 32). [https://doi.org/10.1175/1520-0485\(2002\)032j3145:IVMNTH;2.0.CO;2](https://doi.org/10.1175/1520-0485(2002)032j3145:IVMNTH;2.0.CO;2)
- Crawford, W. R., & Thomson, R. E. (1984). Diurnal-Period Continental Shelf Waves along Vancouver Island: A Comparison of Observations with Theoretical Models. *Journal of Physical Oceanography*, 14(10), 1629–1646. [https://doi.org/10.1175/1520-0485\(1984\)014j1629:dpcswa;2.0.co;2](https://doi.org/10.1175/1520-0485(1984)014j1629:dpcswa;2.0.co;2)
- Cummins, P. F., Masson, D., & Foreman, M. G. G. (2000). Stratification and mean flow effects on diurnal tidal currents off Vancouver Island. *Journal of Physical Oceanography*, 30(1), 15–30. [https://doi.org/10.1175/1520-0485\(2000\)030j0015:SAMFEO;2.0.CO;2](https://doi.org/10.1175/1520-0485(2000)030j0015:SAMFEO;2.0.CO;2)
- D'Asaro, E. A. (1985). The energy flux from the wind to near-inertial motions in the surface mixed layer. *J. Phys. Oceanogr.*, 15(8, Aug. 1985), 1043–1059. [https://doi.org/10.1175/1520-0485\(1985\)015j1043:tefftw;2.0.co;2](https://doi.org/10.1175/1520-0485(1985)015j1043:tefftw;2.0.co;2)
- Drakopoulos, P. G., & Marsden, R. F. (1993). The internal tide off the west coast of Vancouver Island. *Journal of Physical Oceanography*, 23(4), 758–775. [https://doi.org/10.1175/1520-0485\(1993\)023j0758:TITOTW;2.0.CO;2](https://doi.org/10.1175/1520-0485(1993)023j0758:TITOTW;2.0.CO;2)
- Garratt, J. R. (1977). Review of Drag Coefficients over Oceans and Continents. [https://doi.org/10.1175/1520-0493\(1977\)1052.0.CO;2](https://doi.org/10.1175/1520-0493(1977)1052.0.CO;2)

- Garrett, C., & Munk, W. (1979). Internal Waves in the Ocean. In *Ann. Rev. Fluid Mech* (Vol. 11).
- Gemmrich, J., & Klymak, J. M. (2015). Dissipation of internal wave energy generated on a critical slope. *Journal of Physical Oceanography*, 45(9), 2221–2238. <https://doi.org/10.1175/JPO-D-14-0236.1>
- Gonella, J. (1972). A rotary-component method for analysing meteorological and oceanographic vector time series (Vol. 19). Pergamon Press.
- Hendershott, M. C., & Garrett, C. (2018). Internal Tides. In *Geophysical Fluid Dynamics* (No. 6). Retrieved from <https://gfd.whoi.edu/wp-content/uploads/sites/18/2018/03/lecture0621>
- Hotchkiss, F. S., & Wunsch, C. (1982). Internal waves in Hudson Canyon with possible geological implications. *Deep Sea Research Part A, Oceanographic Research Papers*, 29(4), 415–442. [https://doi.org/10.1016/0198-0149\(82\)90068-1](https://doi.org/10.1016/0198-0149(82)90068-1)
- Johnston, T. M. S., & Rudnick, D. L. (2015). Trapped diurnal internal tides, propagating semidiurnal internal tides, and mixing estimates in the California Current System from sustained glider observations, 2006–2012. *Deep-Sea Research Part II: Topical Studies in Oceanography*, 112, 61–78. <https://doi.org/10.1016/j.dsr2.2014.03.009>
- Klymak, J. M., Alford, M. H., Pinkel, R., Lien, R. C., Yang, Y. J., & Tang, T. Y. (2011). The breaking and scattering of the internal tide on a continental slope. *Journal of Physical Oceanography*, 41(5), 926–945. <https://doi.org/10.1175/2010JPO4500.1>
- Kundu, P. K., & Cohen, I. (2008). *Fluid mechanics*. (4th ed.). Academic Press.
- Kunze, E. (2017). Internal-wave-driven mixing: Global geography and budgets. *Journal of Physical Oceanography*, 47(6), 1325–1345. <https://doi.org/10.1175/JPO-D-16-0141.1>
- Kunze, E., Rosenfeld, L. K., Carter, G. S., & Gregg, M. C. (2002). Internal waves in Monterey Submarine Canyon. *Journal of Physical Oceanography*, 32(6), 1890–1913. [https://doi.org/10.1175/1520-0485\(2002\)032;1890:IWIMSC;2.0.CO;2](https://doi.org/10.1175/1520-0485(2002)032;1890:IWIMSC;2.0.CO;2)
- Kunze, E., Mackay, C., Mcphee-Shaw, E. E., Morrice, K., Girton, J. B., & Terker, S. R. (2012). Turbulent mixing and exchange with interior waters on sloping boundaries. *Journal of Physical Oceanography*, 42(6),

- 910–927. <https://doi.org/10.1175/JPO-D-11-075.1>
- Kuroda, H., Kusaka, A., Isoda, Y., Honda, S., Ito, S., & Onitsuka, T. (2018). Diurnal tidal currents attributed to free baroclinic coastal-trapped waves on the Pacific shelf off the southeastern coast of Hokkaido, Japan. *Continental Shelf Research*, 158, 45–56. <https://doi.org/10.1016/j.csr.2018.02.010>
- Lamb, K. G. (2014). Internal wave breaking and dissipation mechanisms on the continental slope/shelf. *Annual Review of Fluid Mechanics*, 46, 231–254. <https://doi.org/10.1146/annurev-fluid-011212-140701>
- Levine, M. D. (2002). A modification of the Garrett-Munk internal wave spectrum. *Journal of Physical Oceanography*, 32(11), 3166–3181. [https://doi.org/10.1175/1520-0485\(2002\)032;3166:AMOTGM;2.0.CO;2](https://doi.org/10.1175/1520-0485(2002)032;3166:AMOTGM;2.0.CO;2)
- Li, M., Myers, P. G., & Freeland, H. (2005). An examination of historical mixed layer depths along Line P in the Gulf of Alaska. *Geophysical Research Letters*, 32(5), 1–4. <https://doi.org/10.1029/2004GL021911>
- Marques, O. B., Alford, M. H., Pinkel, R., MacKinnon, J. A., Klymak, J. M., Nash, J. D., ... Braznikov, D. (2020). Internal Tide Structure and Temporal Variability on the Reflective Continental Slope of South-eastern Tasmania. *Journal of Physical Oceanography*, 51(2), 611–631. <https://doi.org/10.1175/jpo-d-20-0044.1>
- Martini, K. I., Alford, M. H., Kunze, E., Kelly, S. M., & Nash, J. D. (2013). Internal bores and breaking internal tides on the Oregon continental slope. *Journal of Physical Oceanography*, 43(1), 120–139. <https://doi.org/10.1175/JPO-D-12-030.1>
- Mihaly, S. F., Thomson, R. E., & Rabinovich, A. B. (1998). Evidence for non-linear interaction between internal waves of inertial and semidiurnal frequency. *Geophysical Research Letters*, 25(8), 1205–1208. <https://doi.org/10.1029/98GL00722>
- Munk, W., & Garrett, C. (1979). Internal Waves and Small-Scale Processes. In C. Wunsch (Ed.), *Evolution of Physical Oceanography*.
- Nash, J. D., Kunze, E., Toole, J. M., & Schmitt, R. W. (2004). Internal tide reflection and turbulent mixing on the continental slope. In *Journal of Physical Oceanography* (Vol. 34). [https://doi.org/10.1175/1520-0485\(2004\)034;1117:ITRATM;2.0.CO;2](https://doi.org/10.1175/1520-0485(2004)034;1117:ITRATM;2.0.CO;2)

- Polzin, K. L., & Lvov, Y. V. (2011). Toward regional characterizations of the oceanic internal wavefield. *Reviews of Geophysics*, 49(4), 4003. <https://doi.org/10.1029/2010RG000329>
- Robertson, R., Dong, J., & Hartlipp, P. (2017). Diurnal Critical Latitude and the Latitude Dependence of Internal Tides, Internal Waves, and Mixing Based on Barcoo Seamount. *Journal of Geophysical Research: Oceans*, 122(10), 7838–7866. <https://doi.org/10.1002/2016JC012591>
- Subeesh, M. P., Unnikrishnan, A. S., & Francis, P. A. (2021). Generation, propagation and dissipation of internal tides on the continental shelf and slope off the west coast of India. *Continental Shelf Research*, 214. <https://doi.org/10.1016/j.csr.2020.104321>
- Terker, S. R., Girton, J. B., Kunze, E., Klymak, J. M., & Pinkel, R. (2014). Observations of the internal tide on the California continental margin near Monterey Bay. *Continental Shelf Research*, 82, 60–71. <https://doi.org/10.1016/j.csr.2014.01.017>
- Thomson, R. E., & Crawford, W. R. (1982). The Generation of Diurnal Period Shelf Waves by Tidal Currents in: *Journal of Physical Oceanography* Volume 12 Issue 7 (1982). *Journal of Physical Oceanography*, 12(7).
- Thomson, R. E., Roth, S. E., & Dymond, J. (1990). Near-inertial motions over a mid-ocean ridge: Effects of topography and hydrothermal plumes. *Journal of Geophysical Research*, 95(C5), 7261. <https://doi.org/10.1029/jc095ic05p07261>
- Thomson, R. E., & Fine, I. V. (2003). Estimating mixed layer depth from oceanic profile data. *Journal of Atmospheric and Oceanic Technology*, 20(2), 319–329. [https://doi.org/10.1175/1520-0426\(2003\)020;0319:EMLDFO;2.0.CO;2](https://doi.org/10.1175/1520-0426(2003)020;0319:EMLDFO;2.0.CO;2)
- Thomson, R. E., & Emery, W. J. (2014). Data Analysis Methods in Physical Oceanography: Third Edition. In *Data Analysis Methods in Physical Oceanography: Third Edition (Third)*. <https://doi.org/10.1016/C2010-0-66362-0>
- Thomson, R. E., & Krassovski, M. V. (2015). Remote alongshore winds drive variability of the California Undercurrent off the British Columbia-Washington coast. *Journal of Geophysical Research: Oceans*, 120(12), 8151–8176. <https://doi.org/10.1002/2015JC011306>
- Voelker, G. S., Olbers, D., Walter, M., Mertens, C., & Myers, P. G. (2020). Estimates of wind power and radiative near-inertial internal wave flux: The

- hybrid slab model and its application to the North Atlantic. *Ocean Dynamics*, 70(11), 1357–1376. <https://doi.org/10.1007/s10236-020-01388-y>
- Xie, X., & Chen, D. (2021). Near-surface reflection and nonlinear effects of low-mode internal tides on a continental slope. *Journal of Physical Oceanography*, 51(4), 1037–1051. <https://doi.org/10.1175/JPO-D-20-0197.1>
- Xie, X., Liu, Q., Zhao, Z., Shang, X., Cai, S., Wang, D., & Chen, D. (2018). Deep Sea Currents Driven by Breaking Internal Tides on the Continental Slope. *Geophysical Research Letters*, 45(12), 6160–6166. <https://doi.org/10.1029/2018GL078372>
- Zheng, J., Tian, J., & Liang, H. (2017). Observation of near-inertial internal waves on the continental slope in the northwestern South China Sea. *Journal of Ocean University of China*, 16(2), 184–190. <https://doi.org/10.1007/s11802-017-3153-7>